PHYSICAL REVIEW D **93,** 104002 (2016)

Moving closer to the collapse of a massless scalar field in spherically symmetric anti–de Sitter spacetimes

Daniel Santos-Oliván and Carlos F. Sopuerta

Institut de Ciències de l'Espai (CSIC-IEEC), Campus UAB, Carrer de Can Magrans s/n, 08193 Cerdanyola del Vallès, Spain

(Received 11 March 2016; published 2 May 2016)

We present a new hybrid Cauchy-characteristic evolution scheme that is particularly suited to study gravitational collapse in spherically symmetric asymptotically (global) anti-de Sitter (AdS) spacetimes. The Cauchy evolution allows us to track the scalar field through the different round trips to the AdS boundary, while the characteristic method can bring us very close to the point of formation of an apparent horizon. We describe all the details of the method, including the transition between the two evolution schemes and the details of the numerical implementation for the case of massless scalar fields. We use this scheme to provide more numerical evidence for a recent conjecture on the power law scaling of the apparent horizon mass resulting from the collapse of subcritical configurations. We also compute the critical exponents and echoing periods for a number of critical points and confirm the expectation that their values should be the same as in the asymptotically flat case.

DOI: 10.1103/PhysRevD.93.104002

I. INTRODUCTION

One of the main results in general relativity (GR) is the discovery of critical phenomena in gravitational collapse by Choptuik [1] (see also [2,3]). The evolution of a massless scalar field in spherically symmetric asymptotically flat spacetime has two possible final states: (i) formation of a (Schwarzschild) black hole (BH) and (ii) dispersion of the scalar field with Minkowski (Mink) spacetime as the final state. Choptuik found [1] that near the threshold between these two possibilities, but within BH formation, the behavior of the system exhibits critical phenomena with the BH mass depending on the deviations of a single initial data parameter from a critical value in a universal way (the same for any family of initial configurations and any initial data parameter).

Collapse in Anti-de Sitter (AdS) and asymptotically AdS (AAdS) spacetimes has received significant attention during the last years. A natural question that arises is the stability of the (global) AdS spacetime. Recent abundant activity on this subject has shown an instability in AAdS spacetimes endowed with a real massless scalar field [4,5]. What has been shown is that certain families of initial configurations lead to the formation of an apparent horizon (AH) independently of their total energy. This is due to the AdS causal structure that allows lightlike signals to reach the AdS boundary in a finite time. Then, a scalar field packet, no matter how small its energy, can bounce repeatedly off the AdS boundary, while the nonlinearity of Einstein's equations transfers power from long wavelength components to short wavelength ones until the scalar field packet gets compact enough to form an AH. This instability, in reference to the cascade towards shortwave modes typical in fluids, is called the *turbulent* instability of AdS [4]. In this sense, the AdS boundary provides a boxlike structure to space that is fundamental for the instability. Indeed, studies [6–11] in asymptotically flat spacetimes with an artificial boundary at a finite distance find the same type of instability. A previous study of gravitational collapse in AdS [12] showed that the cosmological constant does not change the properties of the collapse with respect to the asymptotically flat case; in particular, the critical exponent for direct collapse does not change. However, the *turbulent* instability was not identified.

In this paper, we looking at the details of collapse in AAdS spacetimes, i.e., we look at the dynamics of AH formation. This is motivated by the fact that the landscape of gravitational collapse in AAdS spacetimes is much richer than in the case of asymptotically flat spacetimes [4]. This problem is quite challenging from the numerical point of view because the scalar field keeps bouncing between the origin and the AdS boundary, while it develops sharper and sharper profiles until an AH is finally formed. This leads to an infinite series of critical points associated with the number of times that the scalar field has traveled to the AdS boundary before collapsing. Most of the numerical computations done until now to evolve a massless scalar field in spherically symmetric AAdS spacetimes use a Cauchy-type evolution like in Choptuik's work [1], which allows us to follow the different bounces off the AdS boundary. In contrast, a characteristic approach like the one proposed by Goldwirth and Piran [13], although it can potentially get much closer to the formation of an AH than a Cauchy scheme, cannot follow the bounces because the grid covers only a part of the spacetime. In this paper, we combine the best of these two worlds into a new scheme that has three essential ingredients: (i) a Cauchy-based evolution scheme numerically implemented using

pseudospectral methods and a compactified radial coordinate in order to follow the scalar field through all the bounces off the AdS boundary, (ii) construction of initial data on a null slice for the characteristic evolution from the results of the Cauchy evolution, and (iii) a characteristic evolution scheme to follow the scalar field all the way to AH formation. This scheme has already been successfully used in [14], where it was found that in AdS spacetime the AH mass of BHs formed following the evolution of subcritical solutions associated with the nth critical point ($n = 0, 1, \ldots$) follow a power law of the form

$$M_{\mathrm{AH}} - M_g^{n+1} \propto (p_n - p)^{\xi}, \tag{1}$$

where p_n is the critical value of the initial data parameter p for the nth branch, M_g^{n+1} is the corresponding mass gap (minimum mass from subcritical configurations), and $\xi \simeq 0.7$ is the exponent. Moreover, ξ appears to be universal, independent of the initial data family and initial data parameter and the same for all the critical points. In this paper, we give all the details about this hybrid Cauchy-characteristic scheme and its numerical implementation (including validation, convergence properties, and other details about evolution in AAdS spacetimes) and provide new results that make the findings of [14] more robust. Mass gaps also appear in type I critical phenomena [15,16], although in this case there is no an equivalent scaling law. In addition, we compute the scaling exponents of the supercritical configurations confirming the expected result [4] that they are the same as in the asymptotically flat case, i.e., $\gamma \simeq 0.374$.

The plan of this paper is as follows. In Sec. II, we introduce the Einstein-Klein-Gordon (EKG) system of equations, and for the spherical-symmetric case, we adapt them to a Cauchy-type formulation in Sec. II A and to a characteristic formulation in Sec. II B. In Sec. II C, we describe the transition from the Cauchy-type evolution to the characteristic one. In Sec. III, we describe the ingredients of the numerical implementation. In Sec. IV, we show numerical results for the validation of the code, including convergence and some special features arising in AAdS spacetimes. Finally, in Sec. V, using this hybrid Cauchy-characteristic code, we present new numerical results on the dynamics of AH formation.

We use units in which $c = 1$ and $8\pi G_d = d - 1$, where G_d is the $(d+1)$-dimensional Newton's gravitational constant and d is the number of spatial dimensions. A semicolon denotes covariant differentiation with respect to the canonical connection, a dot denotes differentiation with respect to the time coordinate t, $\dot{\phi} \equiv \partial\phi/\partial t$, and differentiation with respect to the compactified radial coordinate x is denoted by a prime, $\phi' \equiv \partial\phi/\partial x$. For other partial derivatives, we use the notation $\partial_y f \equiv \partial f/\partial y \equiv f_{,y}$. We use small-case Greek letters $\alpha, \beta, \ldots = 0, \ldots, d$ for spacetime indices.

II. FIELD EQUATIONS

The field equations for a self-gravitating, real massless scalar field in an AAdS spacetime are the EKG equations for the metric $\mathrm{g}_{\mu\nu}$ and scalar field ϕ,

$$G_{\mu\nu} + \Lambda \mathrm{g}_{\mu\nu} = (d-1)\left(\phi_{;\mu}\phi_{;\nu} - \frac{1}{2}\mathrm{g}_{\mu\nu}\phi_{;\alpha}\phi^{;\alpha}\right), \tag{2}$$

$$\mathrm{g}^{\mu\nu}\phi_{;\mu\nu} = 0, \tag{3}$$

where $G_{\mu\nu}$ is the $(d+1)$-dimensional Einstein tensor and Λ is the (negative) cosmological constant.

We restrict our study to spherically symmetric configurations. This assumption simplifies the structure of the spacetime metric and the field equations. Spherically symmetric spacetimes have a warped geometry, which means that their metric tensor can be written in the form $ds^2 = \mathrm{g}_{AB}(x^C)dx^A dx^B + r^2(x^C)\gamma_{ab}dx^a dx^b$ ($A, B, \ldots = 0, 1$ and $a, b, \ldots = 2, \ldots, d$), where g_{AB} is a Lorentzian metric (with associated manifold M^2), γ_{ab} is the unit curvature metric on the $(d-1)$-sphere (with associated manifold S^{d-1}), and $r = r(x^A)$ is the radial area coordinate. The fact that $r^2(x^C)\gamma_{ab}$ is not a true metric on S^{d-1} is what prevents the spacetime manifold M^{d+1} from being a true product of the two manifolds M^2 and S^{d-1}. Instead, it is said that the spacetime manifold is the warped product of M^2 and S^{d-1}, and this is sometimes denoted in the literature as $M^{d+1} = M^2 \times_r S^{d-1}$.

We can freely choose the coordinates in the Lorentzian manifold M^2. In this work, we consider two different choices according to the type of spacetime slicing that they induce. (i) Timelike slicing: We consider coordinates $(x^A) = (t, x)$ so that the spacetime is sliced in spacelike (with timelike normal) hypersurfaces $\{t = \mathrm{const}\}$. In addition, we take x to be a radial coordinate that compactifies the radial direction so that it is in the range of $x \in [0, \pi/2]$, where $x = 0$ corresponds to the *center* of the radial coordinate system and $x = \pi/2$ corresponds to the AdS boundary. Using these coordinates, we can set up a Cauchy-type system of evolution equations with some constraints. Given the causal structure of AAdS spacetimes, the scalar field can propagate to reach the AdS boundary in a finite time. Previous works on this problem (see, e.g., [4,17]) showed that we can expect the field to bounce off the AdS boundary a number of times and eventually collapse near the center $x = 0$. It is for this reason that we use the compactified coordinate x in order to track the field up to the AdS boundary. The equations are given in Sec. II A. (ii) Lightlike slicing: We consider coordinates $(x^A) = (u, r)$ so that the spacetime is foliated by outgoing null slices (composed by outgoing null rays) $\{u = \mathrm{const}\}$. The radial coordinate r is not a compactified radial coordinate as in the previous case in the sense that the AdS boundary is located at $r \to \infty$. This system of coordinates allows us to set up a characteristic-type system

of evolution of equations. In contrast to the coordinates (t, x), the coordinates (u, r) do not allow us to follow the field up to the AdS boundary. Instead, we want to use them in order to track the evolution of the field near collapse, that is, near the center $r = x = 0$. The fact that the $\{u = \text{const}\}$ slices are outgoing means that as we evolve in u we approach the collapse faster than in the case of the Cauchy evolution. As we will see, the characteristic evolution allows us to get much closer to the formation of an AH than the Cauchy evolution. The equations for this case are given in Sec. II B.

A. Cauchy-type evolution of the EKG system

Following [4,5] and our previous discussion, the metric of an spherically symmetric AAdS spacetime in $d+1$ dimensions can be written as

$$ds^2 = \frac{\ell^2}{\cos^2 x}\left(-Ae^{-2\delta}dt^2 + \frac{dx^2}{A} + \sin^2 x\, d\Omega_{d-1}^2\right), \quad (4)$$

where $d\Omega_{d-1}^2$ is the metric of the unit $(d-1)$-sphere (S^{d-1}), A and δ are the two metric functions that completely determine the metric and depend only on (t, x), and ℓ is the AdS length scale, which is related to the cosmological constant Λ by the expression $\ell^2 = -d(d-1)/2\Lambda$. The time coordinate t has an infinite range, i.e., $t \in (-\infty, \infty)$, where x is a radial compactified coordinate that goes from $x = 0$ (center) to $\pi/2$ (AdS boundary). We can recover AdS spacetime by setting $A = 1$ and $\delta = 0$.

From the field Eqs. (2) and (3), we can derive partial differential equations (PDEs) for A, δ, and ψ (see, e.g., [4]). Since we use a pseudospectral multidomain method (see Appendix B for a summary of the main ingredients) for the Cauchy evolution, we are interested in a first-order formulation of the equations based on the characteristic variables associated with our dynamics (see [18] for a definition of the characteristic variables of a hyperbolic system of PDEs and Appendix A for a derivation of the hyperbolic structure of our equations). In our case, the only true hyperbolic sector is the one corresponding to the Klein-Gordon Eq. (3). The characteristic variables of our system, U and V [see Eq. (A15)], are such that U corresponds to the scalar field mode that propagates always with positive velocity and V to the mode with negative velocity (see Fig. 1). Their expressions in terms of the scalar field are

$$U = \frac{1}{\cos^{d-2} x}\left(\phi' - \frac{e^{\delta}}{A}\dot{\phi}\right), \quad (5)$$

$$V = \frac{1}{\cos^{d-2} x}\left(\phi' + \frac{e^{\delta}}{A}\dot{\phi}\right). \quad (6)$$

It is convenient to introduce the following normalized variable associated with the scalar field,

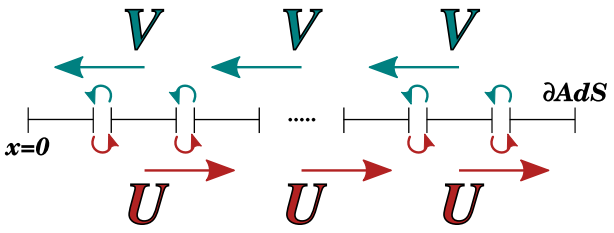

FIG. 1. Diagram of the multidomain structure. The evolution variables need to be communicated between domains using the characteristic variables, U and V, which have a well-defined direction of propagation. The communication is done by copying the boundary values in the direction indicated by the arrows.

$$\psi = \frac{\phi}{\cos^{d-1} x}. \quad (7)$$

Then, from the field Eqs. (2) and (3), we derive the PDEs for (ψ, U, V, A, δ). (i) Evolution equations:

$$\dot{\psi} = \frac{Ae^{-\delta}}{2\cos x}(V - U), \quad (8)$$

$$\dot{U} = -Ae^{-\delta}U_{,x} - \frac{(d - 2\cos^2 x)}{\sin x \cos x}Ue^{-\delta}(1 - A) - \frac{1}{2}\frac{(d-1)Ae^{-\delta}}{\sin x \cos x}(U + V) + (d-2)\frac{\sin x}{\cos x}UAe^{-\delta}, \quad (9)$$

$$\dot{V} = Ae^{-\delta}V_{,x} + \frac{(d - 2\cos^2 x)}{\sin x \cos x}Ve^{-\delta}(1 - A) + \frac{1}{2}\frac{(d-1)Ae^{-\delta}}{\sin x \cos x}(U + V) - (d-2)\frac{\sin x}{\cos x}VAe^{-\delta}, \quad (10)$$

$$\dot{A} = -\frac{1}{2}A^2 e^{-\delta}\sin x \cos^{2d-3} x(V^2 - U^2), \quad (11)$$

(ii) Constraint equations[1]:

$$A' = \frac{d - 2 + 2\sin^2 x}{\sin x\, \cos x}(1 - A) - \frac{A}{2}\sin x \cos^{2d-3} x(V^2 + U^2), \quad (12)$$

$$\delta' = -\frac{1}{2}\sin x \cos^{2d-3} x(V^2 + U^2). \quad (13)$$

It is interesting to note that we have an evolution and a constraint equation for A. As we have already indicated, only the scalar field sector has a hyperbolic structure, Eqs. (9) and (10), while the evolution of A does not contain any gradients of the variables. In practice, we can solve for

[1]The distinction between evolution and constraint equations we make here is not in correspondence with the evolution and constraint equations of the $3+1$ ADM formalism [19].

A either by evolving it using Eq. (11) or by solving the *elliptic* Eq. (12). On the other hand, from the definition of U and V, Eqs. (5) and (6), we can find a constraint equation for the scalar field ϕ,

$$\phi' = \frac{1}{2}\cos^{d-2}x(U+V), \tag{14}$$

and therefore also for the normalized scalar field ψ,

$$\psi' = \psi\frac{\sin x}{\cos x}(d-1) + \frac{1}{2}\frac{U+V}{\cos x}. \tag{15}$$

Then, like in the case of A, we can solve for ψ either by evolving Eq. (8) or by solving this constraint equation.

To solve these equations, we need boundary conditions at the center $x=0$ and at the AdS boundary $x=\pi/2$. Near $x=0$, we find that the scalar field variables have the following power expansion:

$$\psi = \psi_0 + \psi_2 x^2 + O(x^4), \tag{16}$$

$$U = U_0 + U_1 x + U_2 x^2 + O(x^3), \tag{17}$$

$$V = -U_0 + U_1 x - U_2 x^2 + O(x^3), \tag{18}$$

and the metric functions have the following expansions:

$$A = 1 + A_2 x^2 + O(x^4), \tag{19}$$

$$\delta = \delta_0 + \delta_2 x^2 + O(x^4), \tag{20}$$

where δ_0 is a time-dependent quantity always greater than zero.

We can also obtain a power expansion near the AdS boundary by just introducing a coordinate change in the radial direction $\rho = \pi/2 - x$. Then, the expansions for the normalized scalar field ψ and the characteristic variables U and V are

$$\psi = \psi_1\rho + O(\rho^3), \tag{21}$$

$$U = U_1\rho + U_2\rho^2 + O(\rho^3), \tag{22}$$

$$V = U_1\rho - U_2\rho^2 + O(\rho^3), \tag{23}$$

and for the metric functions A and δ are

$$A = 1 + O(\rho^d), \tag{24}$$

$$\delta = O(\rho^{2d}). \tag{25}$$

B. Characteristic-type evolution of the EKG system

For the characteristic evolution, we adapt the scheme used in [13,20] to the case of AAdS spacetimes with spherical symmetry. The form of the metric is

$$ds^2 = -g\bar{g}\,du^2 - 2g\,du dr + r^2 d\Omega^2_{d-1}, \tag{26}$$

where u is an outgoing null coordinate ($u=$ const. is an outgoing null geodesic) and r is the radial area coordinate. The coordinate range for (u,r) is $u\in(-\infty,\infty)$ and $r\in(0,+\infty)$ (although the range of r depends on whether and where gravitational collapse takes place). The AdS boundary corresponds to $r\to\infty$. The functions $g=g(u,r)$ and $\bar{g}=\bar{g}(u,r)$ are always greater than some normalization value at the origin that we choose to be unity. The AdS limit is $g\to 1$ and $\bar{g}\to 1+r^2/\ell^2$. The coordinates (u,r) have dimensions of length, and throughout this paper, the numerical values that we quote are in units of the length scale ℓ.

To write the field Eqs. (2) and (3) in the coordinates of Eq. (26), we introduce two variables associated with the scalar field ϕ,

$$\bar{h} = \phi, \tag{27}$$

and

$$\frac{d-1}{2}r^{\frac{d-3}{2}}h = (r^{\frac{d-1}{2}}\bar{h})_{,r}. \tag{28}$$

Then, we can recover $\bar{h}$ from h by integration as follows:

$$\bar{h}(u,r) = \frac{d-1}{2}r^{\frac{1-d}{2}}\int_0^r r'^{\frac{d-3}{2}}h(u,r')dr'. \tag{29}$$

Moreover, from the (r,r) and (u,r) components of the Einstein Eq. (2) for the metric of Eq. (26), we get

$$g_{,r} = rg(\bar{h}_{,r})^2, \tag{30}$$

$$(r^{d-2}\bar{g})_{,r} = \left(d-2+d\frac{r^2}{l^2}\right)r^{d-3}g, \tag{31}$$

and from here, we can solve for the metric variables $(g,\bar{g})$ in terms of the scalar field variables $(h,\bar{h})$ as

$$g(u,r) = \exp\left\{\frac{(d-1)^2}{4}\int_0^r dr'\frac{(h(u,r')-\bar{h}(u,r'))^2}{r'}\right\}, \tag{32}$$

$$\bar{g}(u,r) = \frac{1}{r^{d-2}}\int_0^r dr'\left(d-2+d\frac{r'^2}{\ell^2}\right)r'^{d-3}g(u,r'). \tag{33}$$

That is, as expected, we can find all the variables of the problem from h. An important observation about Eq. (33) is that both the numerator and denominator of the right-hand side go to zero as we approach the origin $r=0$, although they do it in a way that the limit is well defined and finite. However, this can problematic from the point of view of the convergence of a numerical algorithm. Then, following

[21] and [22], we can get an alternative form for this equation by using integration by parts. The result is

$$\bar{g}(u,r) = \left(1+\frac{r^2}{\ell^2}\right) g(u,r) - \frac{(d-1)^2}{4r^{d-2}} \int_0^r dr' r'^{d-3} \left(1+\frac{r'^2}{\ell^2}\right) \times (h(u,r') - \bar{h}(u,r'))^2 g(u,r'), \quad (34)$$

where we have used the boundary conditions at the origin and the equation for $g(u,r)$ [Eq. (32)]. Now, the second term in this equation goes to zero as we approach the origin, and hence, it is more amenable for numerical computations. The only remaining equation is the one for h, which can be obtained from the Klein-Gordon Eq. (3),

$$\frac{\partial^2 \bar{h}}{\partial u \partial r} - \frac{1}{2}\frac{\partial}{\partial r}\left(\bar{g}\frac{\partial \bar{h}}{\partial r}\right) + \frac{d-1}{2r}\left(\frac{\partial \bar{h}}{\partial u} - \bar{g}\frac{\partial \bar{h}}{\partial r}\right) = 0. \quad (35)$$

Using Eq. (28), the equation for h is

$$\frac{\partial h}{\partial u} - \frac{1}{2}\bar{g}\frac{\partial h}{\partial r} = \frac{h-\bar{h}}{2r}\left[\left(d-2+d\frac{r^2}{\ell^2}\right)g - \frac{d-1}{2}\bar{g}\right]. \quad (36)$$

In this work, we use the characteristic initial value problem in the traditional way, integrating the hyperbolic equations along their associated characteristic lines (see, e.g., [18,23]). Then, we set up initial data on an initial outgoing null slice $\{u = u_o = \text{const}\}$ and evolve that data onto the next slice $\{u = u_o + \Delta u = \text{const}\}$ through the ingoing null geodesics (the purple lines in Fig. 2), which are given by

$$\frac{dr}{du} = -\frac{1}{2}\bar{g}. \quad (37)$$

Integrating along the ingoing null geodesics allows us to exchange partial derivatives of our variables by total derivatives with respect to u. For instance, in the case of the field variable h, we have

$$\frac{dh(u,r(u))}{du} = \left(\frac{\partial h}{\partial u}\right)_{r=r(u)} + \left(\frac{\partial h}{\partial r}\right)_{r=r(u)} \frac{dr(u)}{du}, \quad (38)$$

where $r(u)$ is an ingoing null geodesic, solution of Eq. (37). In this way, we can replace Eq. (36) by ordinary differential equations, one for the variable h,

$$\frac{dh}{du} = \frac{h-\bar{h}}{2r}\left[\left(d-2+d\frac{r^2}{\ell^2}\right)g - \frac{d-1}{2}\bar{g}\right], \quad (39)$$

and another one for $r(u)$, namely, Eq. (37). The first one, Eq. (39), tells us how to evolve h from a $\{u = \text{const}\}$ slice to the next one. The second one tells us that the coordinate r of a point in a $\{u = \text{const}\}$ slice changes following its own ingoing null radial geodesic.

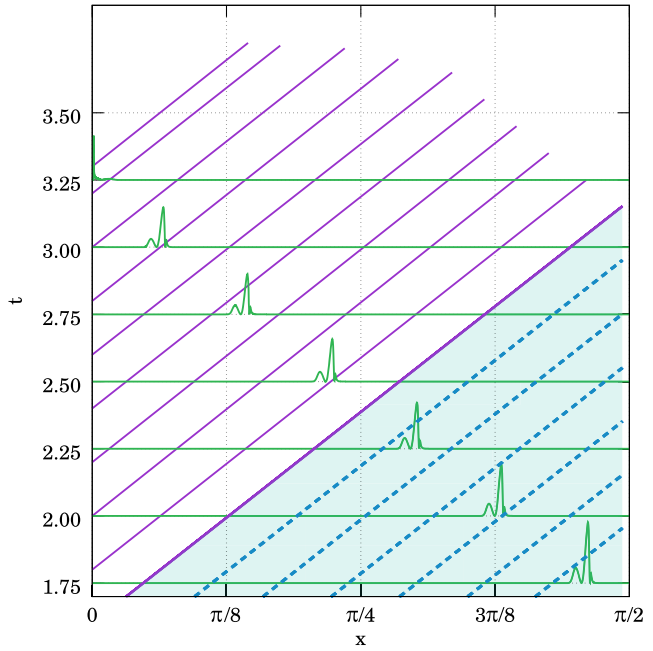

FIG. 2. Characteristic evolution. The green (mostly horizontal) lines represent the energy density as computed using the Cauchy evolution at different times (evolution goes in the vertical time direction). Blue dashed lines are characteristics (outgoing null geodesics) computed through the Cauchy data. Purple lines represent the null *surfaces* we have evolved using the characteristic scheme, with the thickest purple line being the initial one. The characteristic grid moves according to Eq. (37), and therefore, the range in r covered decreases over time.

Some of the previous expressions can be problematic at $r = 0$. To evaluate them there, we need to understand the behavior of our variables around $r = 0$. Assuming the following expansion for the scalar field $\phi = \bar{h}$,

$$\bar{h} = \phi_0 + \phi_1 r + \phi_2 r^2 + O(r^3), \quad (40)$$

we obtain the following expansions for the rest of variables:

$$h = \phi_0 + \frac{d+1}{d-1}\phi_1 r + \frac{d+3}{d-1}\phi_2 r^2 + O(r^3), \quad (41)$$

$$g = 1 + \frac{1}{2}\phi_1^2 r^2 + O(r^3), \quad (42)$$

$$\bar{g} = 1 + O(r^2). \quad (43)$$

C. Transition from the Cauchy evolution to the characteristic evolution

During the Cauchy evolution, we can monitor our variables to see when we approach the collapse. Then, at that point, we can make the transition from the Cauchy

evolution of Sec. II A to the characteristic evolution of Sec. II B in order to follow better the dynamics near collapse. This transition consists in constructing initial data on an initial null slice $\{u = u_o = \text{const}\}$ from the outcome of the Cauchy evolution. It is important to cover a portion of the spacetime that guarantees that the characteristic evolution will cover the formation of the AH. This is illustrated in Fig. 2, where the first purple line (a null outgoing geodesic) indicates the initial slice that we choose for the characteristic evolution. As we can see, the initial data on that slice uses the information from the Cauchy evolution corresponding to an evolution time of $t_f - t_i \approx \pi/2$, so that AH formation is covered.

This transition requires us to find the relations between different objects of the Cauchy and characteristic evolutions. First, we need to find the relation between the coordinates (t, x), used for the Cauchy evolution and the coordinates (u, r) of the characteristic one. The relation between the radial coordinates x and r is quite straightforward considering the factor in front of the metric of the unit $(d-1)$-sphere in Eqs. (4) and (26), from where we get

$$r = \ell \tan x. \tag{44}$$

The second important ingredient is the construction of the initial null slice for the characteristic evolution from the information extracted from the Cauchy evolution. This can be done by finding the outgoing null geodesics from the Cauchy evolution. From the expression of the metric in Eq. (4), the outgoing null geodesics are given by

$$\frac{dx}{dt} = +Ae^{-\delta} \equiv v(t, x), \tag{45}$$

where the plus sign denotes that these radial null geodesics are outgoing (a minus sign corresponds to ingoing null geodesics). To integrate this ODE, we need the values of the metric functions $A(t, x)$ and $\delta(t, x)$, from the Cauchy evolution over the spacetime region that includes the null geodesics of interest. Some of these geodesics are shown in the $t - x$ diagram in Fig. 2.

The next important ingredient is the construction of initial data for the characteristic evolution on one of the null outgoing geodesics that constitute the slicing $\{u = \text{const}\}$. To begin with, let us apply the coordinate transformation of Eq. (44), adding the transformation $\tau = \ell t$ to the metric in Eq. (4). This brings this metric to a more familiar form,

$$ds^2 = -Ae^{-2\delta}\left(1 + \frac{r^2}{\ell^2}\right)d\tau^2 + \frac{dr^2}{A(1 + \frac{r^2}{\ell^2})} + r^2 d\Omega_{d-1}^2. \tag{46}$$

The AdS limit $A \to 1$ and $\delta \to 0$ gives us the well-known form of the AdS spacetime metric. With this in mind, let us perform a general coordinate transformation from the Cauchy formulation metric to the characteristic formulation metric

$$\tau = \mathcal{F}(u, r), \tag{47}$$

which transforms the metric in Eq. (46) into the metric

$$\begin{aligned} ds^2 = &-Ae^{-2\delta}\left(1 + \frac{r^2}{\ell^2}\right)\mathcal{F}_u^2 du^2 \\ &- 2Ae^{-2\delta}\left(1 + \frac{r^2}{\ell^2}\right)\mathcal{F}_u\mathcal{F}_r du dr \\ &+ \left[1 - A^2 e^{-2\delta}\left(1 + \frac{r^2}{\ell^2}\right)^2 \mathcal{F}_r^2\right]\frac{dr^2}{A(1 + \frac{r^2}{\ell^2})} \\ &+ r^2 d\Omega_{d-1}^2, \end{aligned} \tag{48}$$

where $\mathcal{F}_u \equiv \partial\mathcal{F}/\partial u$ and $\mathcal{F}_r \equiv \partial\mathcal{F}/\partial r$. Now, let us impose two conditions on the general coordinate transformation of Eq. (47). The first one comes from the comparison of this general metric to the characteristic metric of Eq. (26) and the fact that the vector $\partial/\partial r$ is a null vector for the second metric. This imposes the following condition on the general metric of Eq. (48): $g_{rr} = 0$. Also, this translates into the following condition on $\mathcal{F}$:

$$\mathcal{F}_r = \frac{1}{(1 + \frac{r^2}{\ell^2})Ae^{-\delta}}. \tag{49}$$

Here, we have made a sign choice. In the case of ingoing null geodesics, we would have chosen the opposite sign for $\mathcal{F}_r$. The second condition that we impose on the coordinate change has to do with the freedom in rescaling the coordinate u, which is a freedom in the choice of the quantity $\mathcal{F}_u$. Our choice, motivated by the implementation of the Cauchy-characteristic transition, is

$$\mathcal{F}_u = e^{\delta_0}, \tag{50}$$

where δ_0 is the value of the metric function δ at $x = 0 = r$. Now, by comparing the line element in Eq. (48) with the one for the characteristic formulation in Eq. (26) and using the conditions on the function $\mathcal{F}$ given in Eqs. (49) and (50), we find the following relations between (A, δ) and $(\bar{g}, g)$:

$$g = e^{\delta_0 - \delta}, \tag{51}$$

$$\bar{g} = Ae^{\delta_0 - \delta}\frac{1}{\cos^2 x}, \tag{52}$$

$$A = \frac{\bar{g}}{g(1 + \frac{r^2}{\ell^2})}. \tag{53}$$

These are key relations for the construction of the initial slice and for the initial data on that slice. Given that AH

formation in the Cauchy evolution is given by the limit $A \to 0$, from Eq. (53), we have that in the characteristic evolution we can track AH formation by monitoring the right-hand side of this equation using the values of $(r, g, \bar{g})$.

On the other hand, from our particular coordinate change, Eqs. (47), (49), and (50), we have the following relation between τ and u (and r):

$$\begin{aligned}\tau &= u + \ell \int_0^x \frac{dx'}{v(t_+(x'), x')} \\ &= u + \int_0^r \frac{dr'}{(1+\frac{r'^2}{\ell^2}) v(t_+(r'), r')},\end{aligned} \tag{54}$$

where $t_+(x)$ denotes the solution for the outgoing null geodesics, Eq. (45), and v is the function of (t, x) defined there.

Finally, we give the relations between the metric and scalar field variables in both formulations. First, ψ and $\bar{h}$ are, by definition, directly related with the scalar field

$$\bar{h} = \phi = \cos^{d-1} x \psi. \tag{55}$$

The scalar field variable h can be constructed along the outgoing null geodesics in term of the Cauchy variables as follows:

$$\begin{aligned}h &= \bar{h} + \frac{2}{d-1} r \bar{h}_{,r} \\ &= \phi + \frac{2}{d-1} r(x) \left(\frac{\partial x}{\partial r} \partial x + \frac{\partial t}{\partial r} \partial t \right) \phi \\ &= \cos^{d-1} x \left(\psi + \frac{2}{d-1} \sin x V \right),\end{aligned} \tag{56}$$

where we have used Eqs. (6), (28), (44), and (54). It is important to notice that h depends on the scalar field itself, through the variable ψ and the ingoing (negative speed) characteristic variable V [see Eq. (6)] but not on the outgoing (positive speed) characteristic variable U [see Eq. (5)]. The reason for this is that we are doing the characteristic evolution using null slices made out of outgoing null geodesics, and hence, the evolution of h from one slice to the next one takes place along ingoing null geodesics [see Eq. (37)].

In summary, Eqs. (51)–(56) contain all the information we need to construct the initial null slice during the Cauchy evolution, the associated coordinate change, and the initial data to initiate the characteristic evolution. This completes the procedure to perform the transition from the Cauchy evolution to the characteristic one.

III. BASICS OF THE NUMERICAL IMPLEMENTATION

In this section, we describe the basic ingredients for the numerical implementation of the two evolution schemes and the transition between them. In the case of the Cauchy evolution, we use pseudospectral collocation methods with multiple domains, building on previous works that have developed this type of technique for the computation of the self-force in black hole spacetimes [24–26]. For the characteristic evolution, we use the method introduced in [13], consisting of using a null foliation where the points of each slice follow ingoing null geodesics (the *characteristic lines*). Finally, we describe how we store the information from several Cauchy slices in order to construct the initial null slice and initial data for the characteristic evolution.

A. Numerical implementation of the Cauchy evolution

In order to have a precise numerical evolution, we are going to use the pseudospectral collocation (PSC) method (see, e.g., [27–29]) for the space discretization, which in our case means in the radial direction, in the compactified radial coordinate x, to be more precise. The main tools of the PSC method used in this paper are briefly described in Appendix B. In a standard spectral method, the outcome of the spatial discretization of a set of hyperbolic PDEs is a (much larger) set of ODEs for the time-dependent spectral coefficients. Instead, in the PSC method, we obtain a set of ODEs for the time-dependent values of our variables, $\boldsymbol{U} = (U, V, \ldots)$ (which variables are evolved in time depends on the choice of equations since some variables, like A and ψ, can be obtained either by time evolution or by radial integration) at the collocation points, $\{\boldsymbol{U}_i(t) \equiv \boldsymbol{U}(t, x_i)\}$, where the equations are forced to be satisfied exactly. The number of ODEs that we obtain is equal to the total number of variables (N_v) times the number of collocation points (N), i.e., $N \times N_v$. The numerical evolution of the resulting ODEs for the collocation values $\{\boldsymbol{U}_i(t)\}$ is performed using a standard Runge-Kutta 4 (RK4) algorithm (see, e.g., [30,31]).

The great advantage of the PSC method is that for smooth solutions it provides exponential convergence, i.e., the truncation error of the spectral series, which can be approximated as the last spectral coefficient, a_N, decays as e^{-N}. In contrast, the cost of most operations, like derivatives, computation of nonlinear terms, etc., increases as N^2 with the number of collocation points, unless we use a fast Fourier algorithm to transform from the physical space (the collocation values of our variables) to the spectral space (the coefficients of the spectral series for our variables), in which case the cost increases only as $N \log N$. In addition, the Courant-Friedrichs-Lewy (CFL) condition for the stability of the evolution of the PDEs (see, e.g., [32]), in the case of the PSC method, is of the form $\Delta t < C N^{-2}$ (where C is a certain constant), in contrast with the typical

form of standard finite difference schemes for PDEs, where $\Delta t < C' N^{-1}$ and C' is another constant. This is due to the structure of the Lobatto-Chebyshev grid that we use (see details in Appendix B), where the points cluster near the boundaries of the domain. As a consequence, the evolution in the PSC method can be significantly more expensive than in the case of finite difference schemes. A way to alleviate this is to use refinement via a multidomain PSC method. The idea is to adapt the size and number of the domains so that different regions in the radial direction with different resolution requirements are covered by an adequate number of collocation points. We can change the number and size of the different domains along the evolution, following the resolution needs of the problem. The practical implementation of the AMR is described in Sec. III B. Most computations are done at each domain in an independent way. The different domains are connected via the corresponding matching conditions, which depend on the type of equation that each variable satisfies.

The Cauchy evolution allows us to follow the system from its initial conditions to the latest stages, just before the collapse. As we have already mentioned, we can expect the scalar field to travel to the AdS boundary ($x = \pi/2$) several times, and in this sense, using the compactified radial coordinate x gives us control over the whole space. On the other hand, when the scalar field is close to collapse, large gradients will be generated in our variables, and the AMR is crucial in order to guarantee the high-resolution requirements needed to resolve the dynamics.

In Sec. II A, we presented the equations we obtained from Einstein's field equations and from the energy momentum conservation in terms of the Cauchy-type variables, namely, (ψ, U, V, A, δ). Some variables have two equations. For instance, the metric function A can be obtained either by evolving Eq. (11) or by integrating Eq. (12), and the same happens with the scalar field variable ψ [see Eqs. (8) and (15)]. We have numerically implemented several combinations of equations; however, in general, we have obtained the best results and efficiency by evolving in time U and V [with Eqs. (9) and (10)] and then obtaining ψ, A, and δ from radial integration [with Eqs. (15), (12), and (13), respectively].

From Eqs. (12) and (13), we can find an integral expression for the metric functions A and δ,

$$A(t,x) - 1 = -\frac{\cos^d x e^{\delta}}{2\sin^{d-2} x} \int_0^x dy\, e^{-\delta} \sin^{d-1} y \cos^{d-3} y (U^2 + V^2), \tag{57}$$

$$\delta(t,x) = \frac{1}{2} \int_x^{\frac{\pi}{2}} dy\, \sin y \cos^{2d-3} y (U^2 + V^2), \tag{58}$$

and using Eq. (15) for the scalar field,

$$\psi(t,x) = -\frac{1}{\cos^{d-1} x} \int_x^{\pi/2} dy \cos^{d-2} y (U^2 + V^2). \tag{59}$$

On the other hand, we can introduce the energy density

$$\mathcal{E}(t,x) = e^{-\delta} \sin^{d-1} y \cos^{d-3} y \left(\frac{U^2 + V^2}{2} \right), \tag{60}$$

and from it we can compute the energy contained inside a sphere of a given radius x, which we call the mass function,

$$\mathcal{M}(t,x) = e^{\delta} \int_0^x dy\, \mathcal{E}(t,y), \tag{61}$$

which is related to the metric function A by

$$A(t,x) = 1 - \frac{\cos^d x}{\sin^{d-2} x} \mathcal{M}(t,x). \tag{62}$$

Then, the ADM mass is just the limit $\mathcal{M}_{\rm ADM} = \lim_{x \to \pi/2} M(t,x)$. The ADM mass is a constant, that does not depend on time, that we can use in our simulations to check the numerical accuracy. In addition, we can define the following quantity:

$$x_{\rm cm} = \frac{1}{M_{\rm ADM}} \int_0^x dy\, y \mathcal{E}(t,y), \tag{63}$$

which plays the role of a radial *center of mass* in the sense that we can use it to track where the energy is concentrated, which is specially useful when evolving localized scalar field configurations, for instance, those corresponding to the initial conditions given in Eq. (72). There are other possible definitions of a radial center of mass; for instance, we can use the radial position of the minimum of the metric function A, i.e., $x_{\rm min}$, such that $A(x_{\rm min}) = \min(A(x)) \equiv A_{\rm min}$. We compare these two definitions of radial center of mass, $x_{\rm cm}$ and $x_{\rm min}$, in Fig. 3, where their evolution is compared with the evolution of $A_{\rm min}$ for two different sets of initial data, the one given in Eq. (72), which collapses after five round trips to the AdS boundary, and the one given in Eq. (79). As we can see in Fig. 3, for the initial profiles in Eq. (72) (left panel), the differences between $x_{\rm min}$ and $x_{\rm cm}$ are quite small, although $x_{\rm min}$ presents some small abrupt features. These features are more prominent for the more complex initial profile of Eq. (79) (right panel), where the evolution of both $x_{\rm cm}$ and $x_{\rm min}$ is more complex, but $x_{\rm cm}$ appears to be a much smoother indicator to track the evolution of the scalar field profile.

Finally, regarding more technical details of the numerical implementation, it is important to mention that all the operations involving the spatial radial direction, including the integrals, are performed within the framework of the PSC method as briefly described in Appendix B. Another important ingredient of the numerical implementation is how to deal with the multiple domains. In our scheme, the

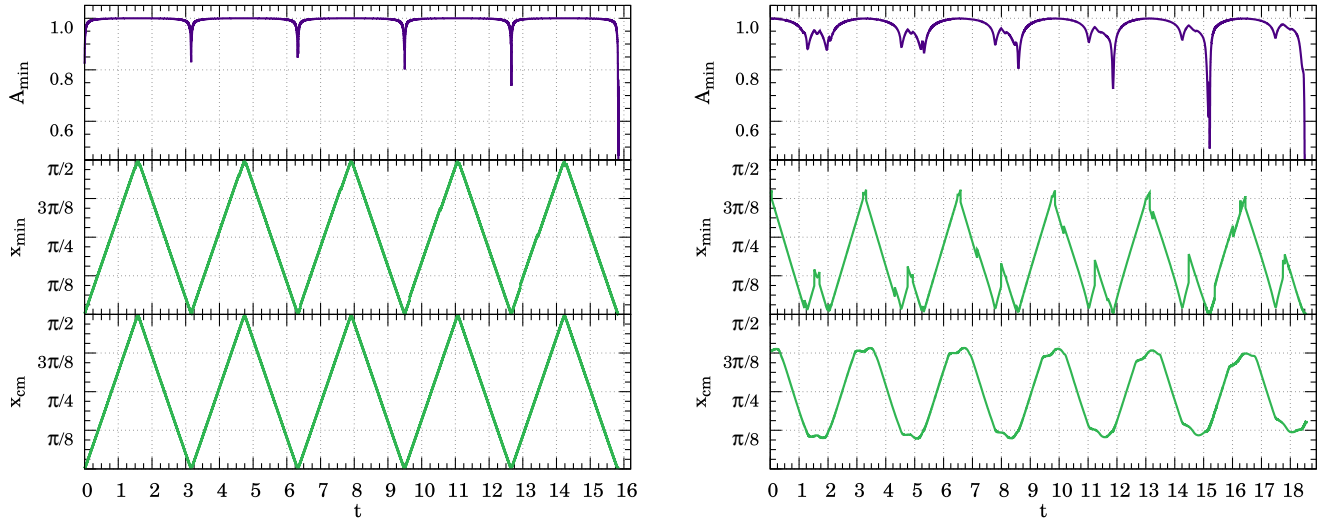

FIG. 3. *Center of mass* evolution. In the left plot, we show the evolution of $A_{\min}$, $x_{\min}$, and x_{cm} for initial conditions in Eq. (72) that collapse after five bounces. In the right plot, we use an initial profile from Eq. (79).

boundaries of each domain have duplicated information because the boundary points of one domain are identified, with the exception of the global boundaries ($x = 0$ and $x = \pi/2$), with the boundary points of the contiguous domains. Although most operations are done locally, at each domain, we need to communicate the different domains through these boundary points. This is the main reason why we have introduced the characteristic variables U and V. These variables have always a well-defined direction of propagation (see Appendix A), which is crucial in order to establish the communication between domains. The characteristic variable U always propagates with positive speed (in direction to the AdS boundary), and the characteristic variable V always travels with negative speed (towards the origin). Then, the way to communicate two given contiguous domains during the Cauchy evolution is to take the value of the variable U from the right boundary of the domain to the left and to copy it into the U value of the left boundary of the domain to the right (see Fig. 1) and the equivalent procedure for V. We take the value of the variable V from the left boundary of the domain to the right and copy it into the V value of the right boundary of the domain to the left. This way of communicating the characteristic variables ensures that we will not find discontinuities in our variables across the boundaries during the numerical evolution. In other words, we perform the communication between domains according to the directions of propagation of the information.

B. Adaptive mesh refinement for the Cauchy evolution

The typical scalar field configurations that we consider in this work, which are localized in the radial direction, follow the same evolutionary pattern, already described in Sec. II A. The scalar field attempts to collapse near the origin, but if the initial amplitude is below some threshold, the scalar field disperses towards the AdS boundary. Then, it bounces off the AdS boundary and travels again towards the origin. This sequence is repeated until the scalar field distribution is compact enough to collapse and form an AH. This means that we need to simulate a compact scalar field distribution back and forth, and some of the scalar field variables exhibit growing gradients as the evolution proceeds. In order to track the pronounced features of the scalar field during the evolution in an efficient way, we resort to AMR techniques based on our multidomain PSC approach. The aim is to design a method in which the resolution follows the field during the round trips to the AdS boundary with a minimal loss of precision and without slowing the evolution much. In this sense, it is important to mention that although we know the evolutionary pattern the details can vary significantly as we change the initial conditions. To illustrate this, in Fig. 4, we show the profile of the scalar field variable U at a similar time for two different simulations where collapse happens after one bounce. We see that the shapes are quite different and require different grids in order to resolve them. In Fig. 5, we show the profile of U at three different times of a simulation where collapse takes place after three bounces. The snapshots of these figures are taken when the field is traveling towards the boundary, so most of the energy is concentrated in the U mode (the one propagating to the right as shown in Fig. 1). They illustrate the need for AMR in our simulations. We have developed two AMR methods for our simulations.

1. First approach: Gradient density estimator

The first AMR method for our spectral multidomain grid is based on a functional that we call the *gradient density* functional, defined at each domain as

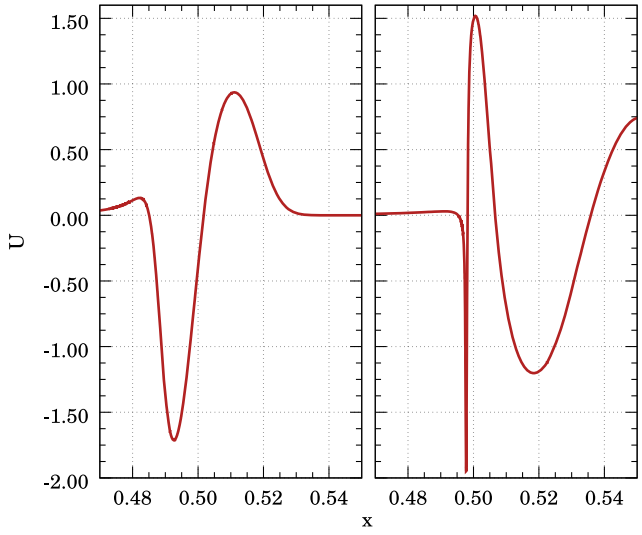

FIG. 4. Cauchy refinement. Comparison between the U profile in two different simulations at a similar time. Both of them are supposed to collapse after one bounce, but the resolution requirements to follow them are very different.

$$\rho_{\mathcal{D}} = \frac{1}{N}\int_{\mathcal{D}} dx|V_{,x}| \geq 0, \tag{64}$$

where $\mathcal{D}$ denotes one of the domains. This indicator is based on the characteristic variable V, and the main idea is to distribute the domain nodes to minimize the gradient density functional. In our numerical experiments, we find a threshold for $\rho_{\mathcal{D}}$ above which the evolution is no longer valid because of the appearance of high-frequency numerical noise. Then, during the simulations, we modify the domain structure to keep $\rho_{\mathcal{D}}$ below that threshold, adding more domains if needed.

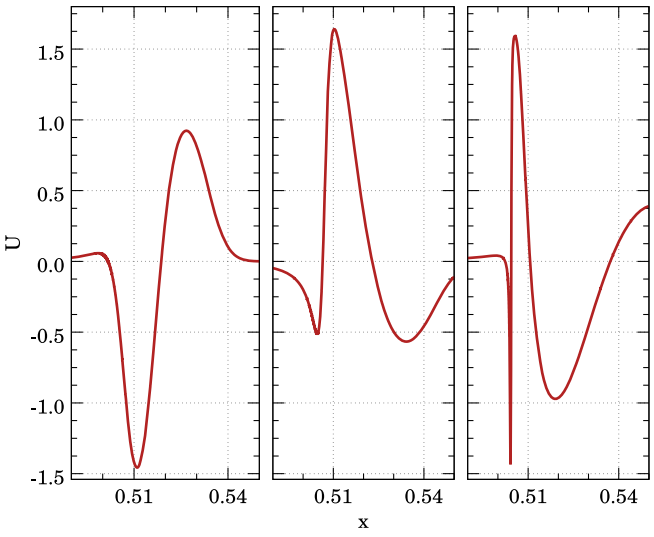

FIG. 5. Cauchy refinement. Comparison between U profiles from the same simulation at different times. This configuration collapses after three bounces. The snapshots are taken at the same position during the trip to the AdS boundary.

This method works reasonably well for capturing the gradients generated during the collapse, but it has several caveats. In particular, it can generate numerical noise far from the region where the scalar field is localized if we do not allow for a minimum resolution there. It can also give problems when the scalar field presents very sharp features that have to be propagated to the AdS boundary and back, which are precisely the most relevant cases for the study of the mass gap in [14].

2. Second approach: Domains over a curve in configuration space

We have developed an alternative method that appears to be more robust for dealing with the most extreme cases where the gradients of variables like U and V, despite being smooth functions, are very large. The starting point is to consider a combination of our Cauchy variables that reflects in a very clear way the regions where more refinement is needed, that is, where we find the largest variations in our variables, let us call it $\gamma(A, \delta, \psi, U, V)$. The length of the curve defined in the plane $[x, \gamma(x)]$, when large gradients in our variables appear, has a large contribution from the relatively small x interval where gradients occur. Then, let us consider the length of this curve from the origin to a certain radial location x,

$$L(x) = \int_0^x d\tilde{x}\sqrt{1+\gamma'(\tilde{x})^2}, \tag{65}$$

where $\gamma' = (\partial\gamma/\partial A)A' + \cdots$. The key idea of this refinement method is to distribute the nodes of our domains so that they cover the same length of the curve $[x, \gamma(x)]$, in contrast with the traditional choice of taking them equally distributed over the x direction. That is, we select the nodes of our domains, $\{\bar{x}_i\}$, as $L(\bar{x}_i) = iL(\pi/2)/D$ $(i = 0, \ldots, D)$, where D is the total number of domains.

In our simulations, we have seen that this method does not require us to establish any threshold, instead we just have to change the multidomain structure after a certain number of time steps to adapt to the changes in the variables in a smooth way. Every time we change the domain structure, we have to interpolate the variables into the new grid. The interpolation between the old and new grids is performed via the pseudospectral representation (see Appendix B for details), and in this way, the numerical error introduced is relatively small.

The specific choice of the function γ is the key ingredient of this method and is quite flexible in the sense that we can tune this choice to the type of initial scalar field profiles or even to the particular state of the numerical evolution. For not very demanding simulations, in terms of gradients of our variables, we can choose γ to be just A, and this provides a very good performance. For more demanding

simulations, a better choice is the scalar field characteristic variable U, when the field is traveling to the AdS boundary, and V, when it is traveling towards the origin. This is motivated by the character of these variables (see Sec. III A). Here, U is the eigenfunction that captures the movement with positive velocity, and V is the one that captures the movement with negative velocity. In practice, we have seen that these simple choices work quite well and allow us to resolve the large changes in these variables that appear during the collapse in the most extreme cases.

C. Numerical implementation of the characteristic evolution

The characteristic evolution described in Sec. II B is completely different from the Cauchy one. We need to set a grid on the initial null slice in terms of the radial coordinate r. When we evolve to the next null slice, the r values of each grid point change following the ingoing null geodesics [see Eq. (37)]. This has two main effects. First, our last grid point (largest value of r, $r_{\max}$) evolves making our physical computational domain shrink, as we show in Fig. 2. Second, the points near the origin are swallowed because according to the equation for ingoing null geodesics these points should evolve to negative values of r, which do not have a well-defined physical meaning. This means that we need to control the size of our grid and be careful with the computations near the origin, but other than that, the characteristic evolution is not problematic. Actually, the reduction of the grid as we proceed with the evolution helps to focus our numerical resolution around the region where the collapse takes place so that we do not need mesh refinement methods in this case. In the cases where the collapse does not occur, we see that the field gets scattered towards infinity as it would do in the asymptotically flat case [13,20]. However, since we are considering AAdS spacetimes, the scalar field has to reach the AdS boundary in a finite time, but the region around the AdS boundary is not covered by our characteristic grid. This means that we have made the transition from the Cauchy to the characteristic evolution too early, and therefore, we need to continue the Cauchy evolution until we can construct an initial null slice whose evolution covers the collapse.

To set up our initial characteristic grid, it is very important to establish its coordinate size, determined by $r_{\max}$, which is the r coordinate of the last grid point. Once this is done, we can freely distribute the other points. A uniform distribution of the grid points in the radial coordinate r is not a good choice because of the CFL condition. For the characteristic evolution, the CFL condition implies

$$\Delta u < \frac{1}{2}\min\left(\frac{r_i - r_{i-1}}{\bar{g}_i}\right), \tag{66}$$

where r_i and r_{i-1} are two contiguous grid points and $\bar{g}_i = \bar{g}(r_i)$. If we have a uniform grid, $r_i - r_{i-1} = \Delta r$ is the same for any i. But when we go to large values of r, we have that the metric function $\bar{g}$ behaves as in pure AdS spacetime (because the field is mostly concentrated near $r = 0$), that is, $\bar{g} \sim r^2$. This means that the CFL condition in this case is controlled by the outer grid points, the ones with largest r, where Δu should be too small. But on physical grounds, it should be the opposite; the CFL condition should be dominated by the points where we need more resolution, around the region where the AH forms. What we do is construct a grid where the grid point separation is constant with respect to the radial coordinate x instead of r; thus, the outer points are well separated in r. From the Cauchy evolution, we extract the values of the scalar field variable h at the different grid points, and from the values of h, we find the other variables, $\bar{h}$, g, and $\bar{g}$, by integration [using Eqs. (29)–(33) or Eq. (34)]. The first grid point for integration is the origin, where we need to prescribe the boundary conditions

$$\bar{h}(r=0) = h(r=0), \qquad \bar{g}(r=0) = g(r=0) = 1. \tag{67}$$

The integration proceeds to the next grid points by using Simpson's rule,

$$\begin{aligned} I_i &\equiv \int_0^{r_i} dr\, f(r) \\ &= I_{i-1} + \frac{r_i - r_{i-1}}{6}[f(r_{i-1}) + 4f(r_M) + f(r_i)], \end{aligned} \tag{68}$$

where $r_M \equiv (r_i + r_{i-1})/2$ is the r coordinate of the midpoint between r_i and r_{i-1}, where the value of the integrand is evaluated using spline interpolation [33].

Each grid point evolves according to the ODE system of Eqs. (39) and (37). To that end, we use again a standard RK4 algorithm (see Refs. [30,31]).

IV. CODE VALIDATION

In this section, we show the performance of the different pieces of the numerical code that we have developed to implement the Cauchy-characteristic scheme described in the previous sections to study gravitational collapse in spherically symmetric AAdS spacetimes.

A. Convergence analysis for the Cauchy evolution

The Cauchy evolution uses a PSC discretization method for the radial direction with multiple domains. At each domain, we use a Chebyshev-Lobatto grid (with linear mapping to the physical radial space; see Appendix B for details). The PSC method provides two representations for each variable, the spectral representation typical of general spectral methods and the *physical* representation, where the values of our variables at the collocation points are the unknowns to be found numerically. The truncation error, the difference between the true values of our variables and their numerical approximation, is given by the terms of the spectral series that we neglect by truncating it. We can

estimate the truncation error by the absolute value of the last spectral coefficient, $|a_N|$ (see, e.g., [27]). For smooth functions, the convergence rate of the Chebyshev series is exponential [27] (spectral convergence), i.e., the truncation error drops exponentially with the number of collocation points. We check convergence for our Cauchy evolution code by performing a series of runs with the same number of domains ($D = 50$), uniformly distributed in the radial coordinate x, and with no refinement. We set the same initial conditions for all of them, from the family of configurations in Eq. (72), and evolve it for a fixed interval of time ($t_f \approx 2$, i.e., after a bounce off the AdS boundary). Then, we look at the last spectral coefficients for the characteristic variables U and V. Here, we only show results from the domain where these variables present more features, which is, in principle, the most challenging one from the numerical point of view, and we have checked that we obtain equivalent results for the other domains. In Fig. 6, at the upper and middle panels, we show the spectral

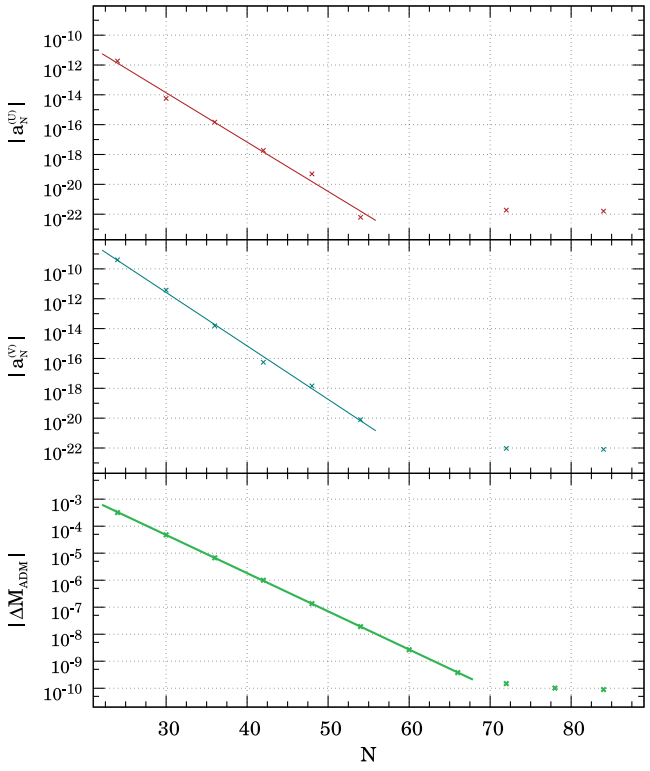

FIG. 6. The upper and middle plots show the truncation error for the variables U and V, $|a_N^{(U)}|$ and $|a_N^{(V)}|$, respectively, as a function of the number of collocation points per domain, N. From all the truncation errors, one at each domain, we take the one where the variables reach their maximum values. The linear fitting with the logarithmic scale in the vertical axis shows the expected exponential convergence (see Sec. IV A). The plot in the bottom shows that deviations in the ADM mass during the evolution also decrease exponentially with the number of collocation points per domain until saturation due to round-off error.

convergence for these two variables in a logarithmic plot of the absolute value of the last spectral coefficient versus the number of collocation points. As we can see, the linear scaling in the logarithmic plot stops at some point, followed by an almost flat profile, indicating that we have reached the round-off error of the computer, and hence, we cannot expect to improve the truncation error any further. In the bottom panel of Fig. 6, we show the variations in the ADM mass, M_{ADM}, with respect to its initial value, $M_{\mathrm{ADM}}(t_0)$, due to numerical inaccuracies during the Cauchy evolution (in an ideal situation, this quantity should vanish for all times). Actually, what we show in this figure is the normalized quantity,

$$\Delta M_{\mathrm{ADM}}(t) = \frac{|M_{\mathrm{ADM}}(t) - M_{\mathrm{ADM}}(t_0)|}{M_{\mathrm{ADM}}(t_0)}. \tag{69}$$

In Fig. 6, we see exponential convergence of the deviations from the ADM mass [$\Delta M_{\mathrm{ADM}}(t_f)$, with $t_0 = 0$] that saturate at a value around 10^{-10} for our particular test runs.

B. Convergence analysis for the characteristic evolution

In the characteristic scheme, we have a nonuniform discretization in the radial coordinate r in the initial grid, and it turns out that the evolution of the r coordinate of the grid points [according to the ingoing null geodesic Eq. (37)] makes our grid even more unequally spaced. Despite of this, the resolution increases with the number of grid points, and we can study how the results converge as we increase this number. To that end, we run simulations with different initial numbers of grid points (the number of grid points changes along the evolution because we lose points through the origin) but with the same initial scalar field profile [see Eq. (76)]. These initial conditions form an AH, and the point of the evolution that we take to analyze the convergence is just before the formation of the AH, when $A = 10^{-8}$ [A is estimated via Eq. (53)]. That is, we monitor how the location of AH formation changes with the number of grid points, N. We use the following indicator:

$$p = \log_2\left(\frac{|r_{\mathrm{AH}}^{N/4} - r_{\mathrm{AH}}^{N/2}|}{|r_{\mathrm{AH}}^{N/2} - r_{\mathrm{AH}}^{N}|}\right). \tag{70}$$

For $N = 120,000$, we obtain $p \approx 3.0034$. This value means that the convergence of our code is third order, in agreement with the convergence rate of the Simpson integration rule that we use.

C. Comparison between the Cauchy and characteristic evolutions

The main reason for implementing a hybrid Cauchy-characteristic evolution scheme is to bring together the best of these two methods of evolution in order to tackle interesting questions about gravitational collapse in

AAdS spacetimes, taking into account that the Cauchy evolution based on the PSC method allows us to follow the possible different bounces of the matter fields (a scalar field in our case) off the AdS boundary with high precision, whereas the characteristic evolution allows us to get very close to the point of formation of an AH. Then, although the two evolution schemes are used in different stages of the evolution, it is interesting to see how they compare when they are applied to the final moments of the collapse, when an AH forms. This comparison is also a justification for the introduction of our hybrid scheme, which on top of the two evolution methods requires a nontrivial transition between them. Then, we have evolved the same scalar field configurations with both evolution schemes to as close as possible to the point of AH formation, which is monitored using the metric function A, which in the characteristic scheme can be computed using Eq. (53). We show the results of this comparison in Fig. 7, where we include a zoom-in plot of the relevant region for AH formation. In the left zoom-in plot, we show the metric function A for a Cauchy evolution until the numerical code is not stable anymore without adding more domains and such that if we keep adding resolution the evolution would essentially freeze because of the tiny time step allowed by the CFL condition. For the right zoom-in plot, we initiated the evolution also with the Cauchy evolution scheme (in order to guarantee that we are comparing the same physical configuration) and then changed to the characteristic scheme until the point where the numerical noise becomes significant or the evolution effectively stops due to a too small Δu step. As we can see, with the characteristic evolution, we can get many orders of magnitude closer to the AH formation than with the Cauchy scheme, as measured in terms of the metric function A. This clearly illustrates the power of our hybrid scheme to study the collapse near AH formation.

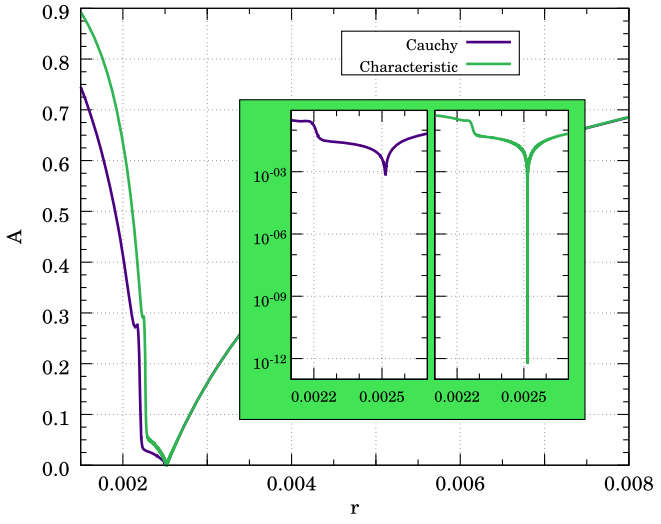

FIG. 7. Comparison of the Cauchy and characteristic evolution methods. We show a snapshot of the function A just before collapse for both cases. The differences are due to the fact that in the first case A is plotted from a $t=$ const slice, while in the second case comes from a $u=$ const slice. The plots coincide around $r=r_{\mathrm{AH}}$. The zoom-in plot shows, by using a logarithmic scale, how close to the AH formation ($A\to 0$) we can get with each evolution scheme.

D. Ingoing null geodesics

In order to understand better the magnitude of the numerical challenge posed by the study of gravitational collapse in AAdS spacetimes, it is interesting to analyze the ingoing null geodesics in the characteristic evolution of AAdS spacetimes and compare them with the ingoing null geodesic in asymptotically flat spacetimes. To begin with, let us look at the difference between the ingoing null geodesics in AdS spacetime, Eq. (26), and in Mink spacetime, in the equivalent coordinate system where the metric has the same form as in Eq. (26). The equation for the ingoing null geodesics has also the same form in both cases, i.e., Eq. (37), but the form of the metric function $\bar{g}$ is different. In AdS spacetime, we have $\bar{g}_{\mathrm{AdS}}(r)=1+r^2/\ell^2$, whereas in Mink we have $\bar{g}_{\mathrm{Mink}}(r)=1$. Therefore, by solving the ingoing null geodesic equation, Eq. (37), we get the following expressions for the ingoing null geodesics:

$$u_{\mathrm{Mink}}(r)=2(r_0-r),$$
$$u_{\mathrm{AdS}}(r)=2(\arctan(r_0)-\arctan(r)). \tag{71}$$

These geodesics have been plotted in Fig. 8. This illustrates what can happen with our characteristic grid in AAdS evolutions in comparison with the asymptotically flat case. As shown in Fig. 8, the grid points of an initial null slice

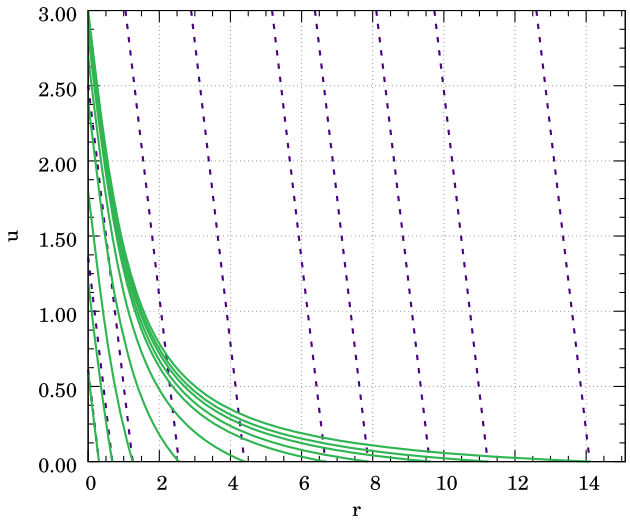

FIG. 8. Comparison of ingoing null geodesics in Mink (dashed purple lines) and AdS (green continuous lines) spacetimes. We see the strong effect that the cosmological constant term has in the geodesics. In AdS spacetime, they reach the region near the origin much faster than in Mink, as measured by the time u.

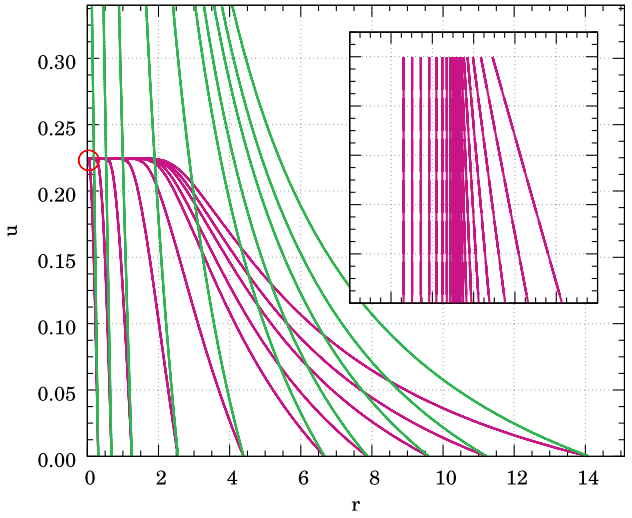

FIG. 9. Comparison between ingoing null geodesics in pure AdS spacetime (green color) and in an AAdS spacetime describing gravitational collapse of a scalar field (fuchsia color). The geodesics focus around the location of AH formation. The small plot is a zoom of the region inside the red circle, where it can be seen how the geodesics behave around $r_{\rm AH}$. This size of the zoom-in plot is $\Delta r \simeq 10^{-4}$ around $r \simeq 0.03952$ and $\Delta u \simeq 10^{-13}$ around $u \simeq 0.224673828858275$.

$(u = 0)$ move towards the origin much faster in AdS spacetime than in Mink spacetime. The conclusion of this for our simulations is that we must be very careful in choosing the initial null slice, in particular, its size, because the grid points in AdS travel very fast towards the region near the origin, which means that our grid shrinks very fast, and we may miss the interesting phenomena, in particular, the formation of an AH.

On the other hand, in Fig. 9, we show the comparison between ingoing null geodesics in AdS spacetime and the ones of an AAdS spacetime, where the scalar field collapses forming an AH. We compute these geodesics numerically as the solution of Eq. (37). As soon as the geodesics approach the spacetime point in the (u, r) plane where the AH forms, all the ingoing null geodesics with $r > r_{\rm AH}$ focus at that point as it can be seen in the zoom-in area of this figure, while those with $r < r_{\rm AH}$ follow a different path.

V. RESULTS FROM THE NUMERICAL EVOLUTION

In this section, we present results of our evolutions of the EKG system, Eqs. (2) and (3), in spherically symmetric AAdS spacetimes. The families of the initial configurations that we use for our evolutions are shown below. Equations (72) and (79) are initial data for Cauchy-only and Cauchy-characteristic evolutions, whereas Eq. (76) shows initial data used for characteristic-only evolutions.

The landscape of the gravitational collapse that emerged after the pioneer work of Ref. [4] can be summarized by saying that initially compact scalar field configurations will sooner or later form an AH. The time required to form the AH depends on how many round trips to the AdS boundary are needed for the AdS *turbulent instability* to convert long-wavelength modes into short-wavelength ones so that the scalar field profile gets compressed enough to form a BH. This is illustrated in Fig. 10, where we show the AH radius, $r_{\rm AH}$, obtained by evolving a number of initial configurations from the family of Eq. (72) with our Cauchy-characteristic evolution scheme. This three-dimensional plot has been obtained by varying both the amplitude, ε, and the width, σ, of the initial configurations. It shows the different branches that appear and that represent configurations that have bounced off the AdS boundary a fixed number of times (indicated by the color and branch number in Fig. 10) before collapsing and forming an AH. This is in contrast with the asymptotically flat case where we have a single branch. The branches are clearly seen in the direction of the amplitude, ε, where we have a high number of points, but it can be seen that it also happens in the direction of the width, σ. The same should happen if we look to any direction in the plane (ε, σ).

In what follows, we describe new results regarding the critical collapse, that is, analyzing the configurations in Fig. 10 near the plane $r_{\rm AH} = 0$, and we also describe results about the mass gap between branches and the power law scaling found in our recent study [14] for the AH mass of the near subcritical configurations. These results consolidate further the conclusions reached in [14].

A. Critical phenomena in AAdS gravitational collapse

In [4], it was concluded that at the critical points separating the branches, the supercritical configurations form an AH with mass going to zero with the same scaling

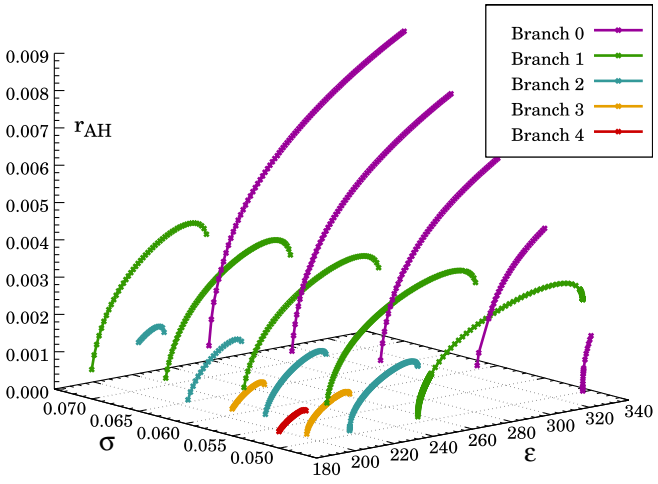

FIG. 10. AH location in a two-parameter phase space. We show the radial location of the AH formed from initial configurations belonging to the family in Eq. (72) for different values of the amplitude, ε, and the width, σ.

as in the case of asymptotically flat spacetimes [1]; that is, $r_{\rm AH} \sim (p - p_n)^{\gamma}$, where p is an arbitrary parameter of the family of initial configurations, p_n is the nth critical value at which the AH mass goes to zero, and γ is an universal exponent that in $d = 3$ has the expected value $\gamma \simeq 0.374$. This conclusion was confirmed in [14] for branch 0 in Fig. 10 by fitting a large number of simulations near the critical point. In the present work, we extend this result for the next five branches (up to branch 5) using the same family of initial data (similar to the one used in [4]):

$$U(t_o, x) = \varepsilon \exp\left(-\frac{4\tan^2 x}{\pi^2 \sigma^2}\right), \qquad V(t_o, x) = -U(t_o, x), \tag{72}$$

that represents a profile centered around the origin at the initial time and characterized by the amplitude, ε, and the width, σ. This particular choice, and any that fulfils the condition $V(t_o, x) = -U(t_o, x)$, directly implies $(\partial_x \phi)(t_o, x) = 0$.

To obtain the scaling of the AH mass near the critical points of the different branches, we have used the method introduced in [34], which consists of following the evolution of subcritical configurations very near the critical point and tracking the behavior of the curvature scalar, R, at the origin ($x = 0$). The subcritical character of these evolutions allows us to perform accurate computations using only the Cauchy evolution. The curvature scalar R at $x = 0$, as well as other curvature scalars, starts to grow when the scalar field attempts to form an AH. It reaches a maximum value (in absolute value), and then it disperses towards the AdS boundary. The maximum value of R is higher the closer we approach the critical point, p_n, being infinite at that point. Actually, it follows a scaling law of the form [34]

$$R_{\rm max}|_{x=0} \sim (p_n - p)^{-2\gamma}. \tag{73}$$

The scalar field near the critical point exhibits discrete self-similarity (type II critical behavior) with an echoing period Δ that for the same reasons we have mentioned for the case of γ should be the same as in the asymptotically flat case, $\Delta \approx 3.44$.

In [35] and [36], it was shown that on top of the scaling of Eq. (73), a finer structure can be seen as oscillations of the form

$$\ln R_{\rm max}|_{x=0} = (-2\gamma)\ln(p_n - p) + b_0 + F(\ln(p_n - p)), \tag{74}$$

where F is a periodic function with period equal to $\Delta/2\gamma$. In terms of the Cauchy evolution variables, the scalar of curvature at the origin can be computed using the following expression:

$$R|_{x=0} = -\frac{12}{\ell^2} - \frac{1}{2\ell^2}(V - U)^2. \tag{75}$$

We have carried out a series of Cauchy evolutions of initial configurations of the family in Eq. (72) with fixed width, $\sigma = 0.05$, and amplitudes chosen in such a way that the configurations are subcritical with respect to any of the first six critical points (see Fig. 10). The results of these simulations are shown in Fig. 11 with the corresponding fittings. The values of the critical amplitudes, ε_n, the critical exponents, γ, and the echoing periods, Δ, are presented in Table I. We can see that the values obtained for γ and Δ are consistent with the known values for the collapse of massless scalar fields in asymptotically flat spacetimes [1,35]. This was already shown for the first branch in [12] and checked in [14].

We have already mentioned that the characteristic method of Sec. II B cannot be used to follow the full evolution of the scalar field because the characteristic grid shrinks with time, and hence, we cannot track bounces of the scalar field off the AdS boundary. However, we can, in principle, use the characteristic evolution for the particular cases in which the scalar field collapses directly, or in other words, we can, in principle, study branch 0 with the characteristic evolution. Actually, this was already done

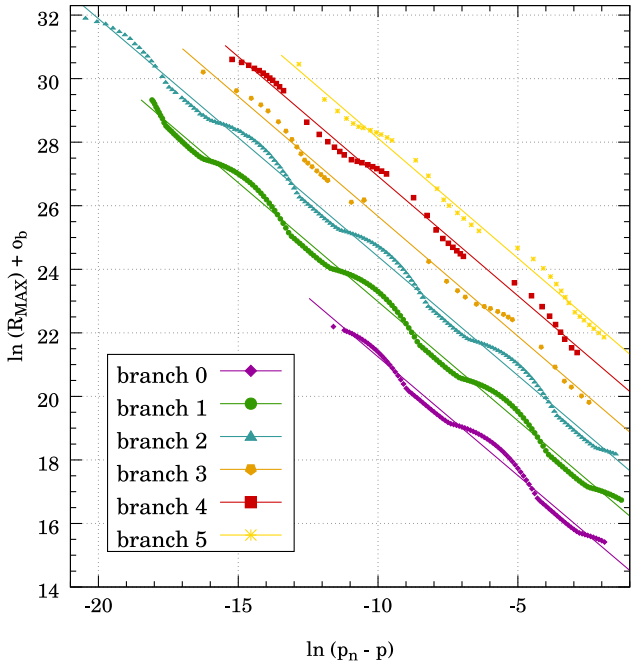

FIG. 11. Critical exponents for fixed width ($\sigma = 0.05$). Scaling of the scalar of curvature, R, for subcritical configuration near the critical point for different branches and from the branch of direct collapse ($b = 0$, bottom) to the branch with five bounces ($b = 5$, top). An offset, o_b, has been added to the y axis to make the plot more clear. The values of the offset are $o_b = -2, -1, 0, +1, +2, +3$, starting from $b = 0$. The results from the fittings are given in Table I.

TABLE I. Critical exponents for fixed width ($\sigma = 0.05$). Fitting values of the critical exponents obtained in Sec. V A correspond to the critical parameters for the six first branches (see Fig. 11).

Branch	Critical value (ε_n)	Critical exponent (γ)	Echoing period (Δ)
$n = 0$	335.572231 ± 0.000005	0.374 ± 0.006	3.33 ± 0.15
$n = 1$	$251.09427729 \pm 0.00000001$	0.3746 ± 0.0008	3.45 ± 0.02
$n = 2$	$216.208077165 \pm 0.000000001$	0.3743 ± 0.0004	3.45 ± 0.02
$n = 3$	$193.9755275 \pm 0.0000001$	0.377 ± 0.007	3.43 ± 0.04
$n = 4$	178.070915 ± 0.000001	0.376 ± 0.007	3.42 ± 0.06
$n = 5$	165.946674 ± 0.000004	0.377 ± 0.010	3.46 ± 0.10

in [12] using a double-null characteristic scheme. Here, we repeat this analysis to confirm this result and, at the same time, to test further our characteristic evolution method. To that end, we have to prescribe initial data on a null slice $u = \text{const}$ for the scalar field variable h. We choose the following family of initial conditions:

$$\phi(r) = \bar{h}(r) = \varepsilon \frac{r^2}{\ell^2} \exp\left(-\frac{(r - r_0)^2}{\ell^2 \sigma^2}\right), \tag{76}$$

which has three parameters: amplitude, ε, width, σ, and center of the profile, r_0, which we always fix to the value $r_0 = 0.1\ell$. We have performed a series of characteristic evolutions varying the amplitude ε for three (fixed) values of the width $\sigma = 0.01$, 0.05, and 0.10. We compute the critical exponent, γ, and echoing period, Δ, from the AH mass, which in AAdS spacetimes with the coordinates of Eq. (26) is given by $M_{\rm AH} = r_{\rm AH}(1 + r_{\rm AH}^2/\ell^2)/2$ (the values of this mass that we quote in this paper are in units of ℓ); that is, we fit our characteristic-only simulations to the formula

$$\ln M_{\rm AH} = \gamma \ln(p - p_n) + b_0 + F(\ln(p - p_n)), \tag{77}$$

where F is again a periodic function with period $\Delta/2\gamma$ [34,35]. The results obtained from these simulations are shown in Fig. 12 with the fittings to Eq. (77). The critical values of the amplitude, ε_0, the critical exponent, γ, and the echoing period, Δ, are given in Table I. Again, the results are consistent with the predictions for the asymptotically flat case.

B. Power law behavior near the mass gaps

The second application of our Cauchy-characteristic evolution scheme is to study the mass gap between the branches of collapsed scalar field configurations (see Fig. 10). In a previous work [14], using this evolution scheme, we found that the subcritical solutions that are very close to the critical points form BHs with an AH whose mass obeys a scaling law of the form

$$M_{\rm AH} - M_g^{n+1} \propto (p_n - p)^{\xi}, \tag{78}$$

where p_n denotes the critical value of the initial data parameter, p, for the nth branch; M_g^{n+1} is the mass of the $(n+1)$th gap, between the branches n and $n+1$, corresponding to the minimum mass of the AH formed by subcritical configurations; and ξ is the power law exponent. In [14], we found that the exponent ξ has a value of $\xi \simeq 0.70$, and it was conjectured that this value is universal, the same for all families of initial configurations and for all branches/critical points. The numerical support for this conjecture given in [14] came from the evolution of two different one-parameter families of initial configurations and for the first two mass gaps, one between branches 0 and 1 and the other between branches 1 and 2. The two one-parameter families of initial configurations both came from the same larger family of initial conditions given in Eq. (72), one by fixing the width σ and the other one by fixing the amplitude ε.

In this work, we give new evidence for this conjecture. We do this by first considering a completely new different

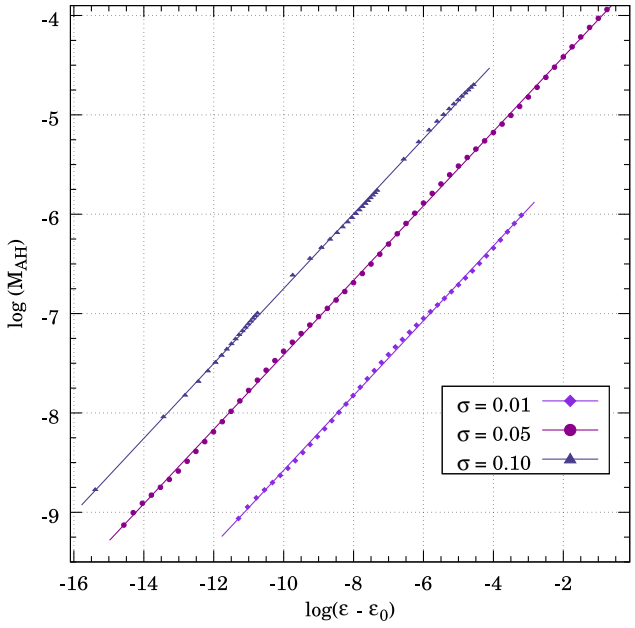

FIG. 12. Critical exponents for branch 0 using the characteristic method. We show the results for the AH mass versus initial amplitude for three different families of initial configurations with fixed width [see Eq. (76)] of branch 0 (direct collapse). The values of the critical amplitudes, critical exponent, and echoing period are given in Table II.

TABLE II. Critical exponents for branch 0 using the characteristic method. Fitting values of the critical exponents obtained in Sec. V A correspond to the critical parameters for the zero branch using the characteristic method (see Fig. 12).

Width (σ)	Critical value (ε_0)	Critical exponent (γ)	Echoing period (Δ)
0.01	7.828039 ± 0.000002	0.376 ± 0.006	3.2 ± 0.4
0.05	$25.907772996 \pm 0.000000003$	0.3748 ± 0.0004	3.33 ± 0.10
0.10	23.8595911 ± 0.0000001	0.375 ± 0.005	3.45 ± 0.10

family of initial configurations, in the sense that it is functionally different, and second by extending the study to the third mass gap between branches 2 and 3.

The new family of initial conditions that we consider is inspired by a proposal in [37] and [38] of setting the initial profile far from the origin and centered close to the AdS boundary. The form for the initial values of our Cauchy variables is given by

$$U(t_o, x) = \varepsilon \cosh^{-1}\left(\frac{\tan(x) - \tan(x_0)}{\sigma}\right),$$
$$V(t_o, x) = -U(t_o, x). \tag{79}$$

This family has three parameters, an amplitude, ε, a width, σ, and the position at which the scalar field profile is centered, x_0, which we always take as a fixed parameter. These configurations are evolved using the Cauchy-characteristic evolution scheme. It turns out that the simulations for the configurations within the parameter region of interest, those that lead to subcritical scalar field collapse, are numerically more challenging than in the case of the initial conditions from the family in Eq. (72). The reason for this is that the energy distribution in the new family of configurations is not as compact as in the old one. This has already been illustrated in the evolutions tracking the *center of mass* of the scalar field profile shown in Fig. 3. For our simulations, we set $x_0 = 1.2$ and $\sigma = 0.2$. With this choice, the first critical point is found at $\varepsilon = \varepsilon_0 = 1.093435 \pm 0.000001$. In Fig. 13, we show, in the plane $\varepsilon - M_{\rm AH}$, the region near this first critical point. The red circle in the figure indicates the area from where we have taken the data to fit the power law of Eq. (78), which is shown in the zoom-in plot of the this figure. In this case, we find that the mass gap is

$$M_g^1 = (7.2954 \pm 0.0008) \times 10^{-3}, \tag{80}$$

and the power law exponent has a value consistent with the conjectured universal character,

$$\xi = 0.68 \pm 0.07. \tag{81}$$

On the other hand, we have also studied the power law of Eq. (78) for additional mass gaps, beyond the gaps between branches 0–1 and 1–2, already studied in [14]. This is a particularly challenging goal since it involves a number of simulations in which we have to track the scalar field through two bounces off the AdS boundary. The difficulty of this problem lies resolution requirements that the subcritical configurations pose on our simulations since we have to evolve the sharp features originated during the quasicollapse stage to the AdS boundary and back. It is also challenging from the point of view of computational cost since each of these simulations takes significantly much more time than the previous ones. We need to perform many of them in order to locate the critical point and to have enough subcritical configurations close to it in order to extract the values of the mass gap and power law exponent with a good precision. Again, considering the conjecture established in [14], we expect to find the same power law [Eq. (78)] around all the mass gaps. We have analyzed the situation around the third mass gap, between branches 2 and 3, using the initial configurations in Eq. (72) fixing the

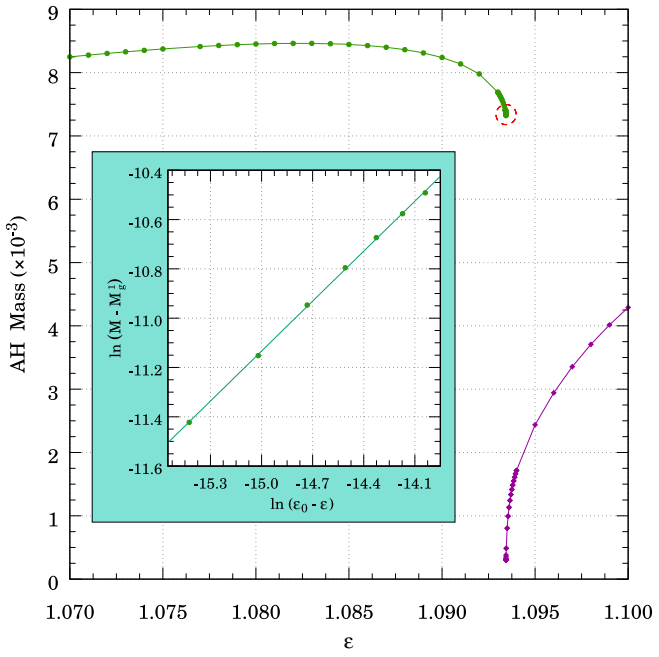

FIG. 13. Mass gap 1, between branches 0 and 1. The behavior near the subcritical solutions marked by the red circle follows the power law in Eq. (78). The zoom-in plot shows the fitting of the data. The critical point is located at an amplitude $\varepsilon_0 = 1.093435 \pm 0.000001$. The values for the mass gap, M_g^1, and power law exponent, ξ, are given in Eqs. (80) and (81), respectively.

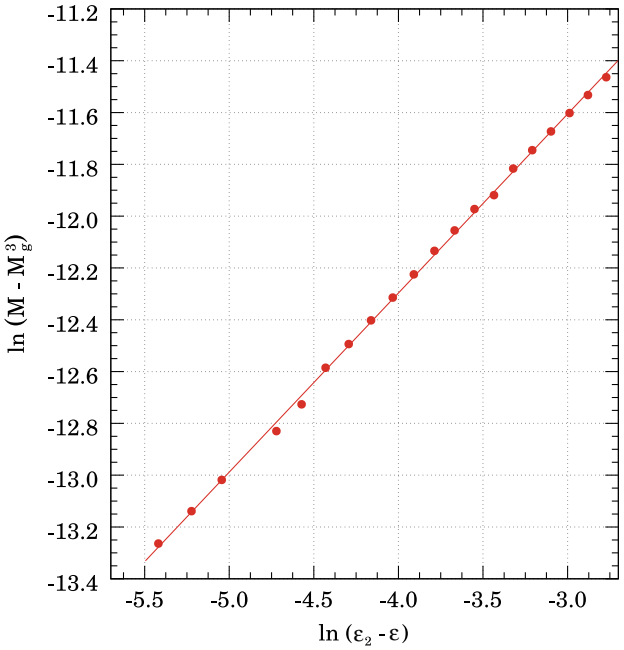

FIG. 14. Subcritical solutions associated with the third mass gap (between branches 2 and 3). The fit of the data to the power law in Eq. (78) is shown. The critical point is found to be located at an amplitude $\varepsilon = \varepsilon_2 = 216.203 \pm 0.009$, and the values for the mass gap, M_g^3, and power law exponent, ξ, are given in Eqs. (82) and (83), respectively.

value of the width to $\sigma = 0.05$. The critical point associated with the second branch is located at a value of $\varepsilon = \varepsilon_2 = 216.203 \pm 0.009$. Then, from the evolution of subcritical configurations associated with this critical point, we obtain the $\varepsilon - M_{\rm AH}$ plot shown in Fig. 14. The fit to this data gives us the value of the mass gap,

$$M_g^3 = (5.44 \pm 0.02) \times 10^{-4}, \tag{82}$$

and the power law exponent of Eq. (78) is found to be

$$\xi = 0.69 \pm 0.04. \tag{83}$$

This value is also consistent with the values found in [14] for the first two mass gaps and with the value found here [see Eq. (81)] for the first mass gap, using a functionally different family of initial data, namely, the one given by Eq. (79). Therefore, these results give more numerical support to the conjecture about the universality of the power law of Eq. (78), with an exponent of $\xi \simeq 0.70$.

VI. CONCLUSIONS

The collapse of a massless scalar field in a spherically symmetric AAdS spacetime shows a much richer phenomenology than the analogous problem in asymptotically flat spacetimes as it was realized for the first time in [4] and is illustrated by our Fig. 10. Both the long-term evolution and the dynamics of gravitational collapse present distinctive features that are not yet fully understood. In this work, we have focussed on the dynamics near collapse, when an AH is forming. To study this question, we need to resort to numerical methods, taking into account that we are dealing with a problem that represents an important challenge for the design and performance of a numerical code that solves the PDEs describing the system, despite the fact that we are dealing with a $1+1$ problem (spherical symmetry). The main reason for this lies behind the causal structure of global AdS, where lightlike signals can reach the AdS boundary in a finite time. As a consequence, a scalar field configurations that fails to form an AH in a first attempt will travel to the AdS in a finite time, bounce, and travel back towards the origin, where it will have a second chance to form an AH. This process will be repeated until after a number of bounces the scalar field will collapse forming an AH. This is not the whole story as we have evidence of the existence of stable scalar field configurations, which makes the whole picture not yet completely understood. The near subcritical configurations are very challenging since they are very close to collapse, which induces large gradients in the field variables that we have to propagate to the AdS boundary and back. In this sense, AAdS spacetimes constitute an excellent arena for the development of new numerical relativity methods and tools.

In this paper, we have presented a new numerical scheme to study these situations which, in essence, is a hybrid Cauchy-characteristic evolution scheme. The Cauchy evolution uses a multidomain PSC method for the spatial discretization, and the characteristic evolution follows the ingoing null geodesics, which allows us to get much closer to the point of AH formation than with the Cauchy evolution. An additional crucial part of this method is the transition between the two schemes. We have described in detail all the analytic and numerical ingredients of this Cauchy-characteristic evolution scheme. In doing so, we have also analyzed the differences between evolution in AAdS and asymptotically flat spacetimes, pointing out how the effect of the cosmological constant makes our simulations more challenging. We have also shown the convergence properties of the different parts of the scheme and how we implement AMR techniques for the Cauchy-evolution sector. Given that the scalar field configurations that we have considered are localized in the radial direction, in the sense that the energy density is concentrated within a single radial interval, we have studied how two definitions of center of mass can track the evolution of the field and how by using them we can also have a sense of how compact a certain scalar field configuration is.

With this numerical scheme, we have studied in [14] the subcritical scalar field configurations near the different branches that appear depending on the number of times that the field bounced off the AdS boundary. We found evidence that these configurations follow the power law

$M_{\rm AH} - M_g^{n+1} \propto (p_n - p)^{\xi}$, with the mass gap between branches (separated by the location of the critical point, p_n) given by M_g^{n+1} and the exponent, ξ, was conjectured to be universal, independent of the initial data and also the same for all the mass gaps/branches. The numerical support provided in [14] comes from the first two mass gaps using the initial conditions of Eq. (72) varying both the amplitude and the width. In this paper, we have found further evidence for this conjecture, first by using a completely different family of initial conditions, the one in Eq. (79), and second by looking at the third mass gap. All these results support our conjecture for the power law at the mass gaps and the universal character of the exponent, which in all cases has been found to be consistent with a value of $\xi \approx 0.7$. It would be interesting to have analytical support for this numerical result, but at a first glance, it appears as a difficult enterprise. The reason is that the subcritical solutions that follow this power law correspond to initial conditions that are very close to those that define the associated critical solution, but they are separated by a full round trip to the AdS boundary. Then, any analytical study of this power law should consider the details of the nonlinear dynamics during the round trip together with the influence of the AdS boundary, which in our view seems even more complicated than the analytical study of the critical solution itself and hence beyond the scope of this paper.

Another open question is the precise role of the AdS boundary. In [9], the introduction of an artificial boundary at a finite distance from the origin in asymptotically flat spacetime leads to a scaling law for the subcritical solutions with the same exponent γ as in the supercritical case. The comparison between their result an ours indicates that there is a difference between global AdS and the system with an artificial boundary in asymptotically flat spacetimes. In this sense, it is interesting to note [39] that our value for the exponent is quite close to $2\gamma \approx 0.74$. Apart from this, the global AdS and the asymptotically flat case with an artificial boundary do not show differences in the structure of the AH phase space (see Fig. 10) nor in the scaling for supercritical configurations. A future interesting study is to look at the case of AdS with an artificial boundary.

On the other hand, we have also obtained the critical exponents associated with the multiple critical points that appear in the case of AAdS spacetimes. By tracking supercritical configurations using only the Cauchy evolution, we have been able to find the critical points associated with branches 0–5. We have confirmed the expected result [4] that at AH formation the presence of the negative cosmological constant is irrelevant. Indeed, the critical exponents and echoing periods that we have found are consistent with the values of the asymptotically flat case.

In summary, we have introduced a hybrid Cauchy-characteristic method that is particularly suited to study the dynamics in spherically symmetric spacetimes near the point of formation of an AH. This has allowed us to find new features and understand better gravitational collapse in AAdS spacetimes. This evolution scheme is quite general, and it can be applied to other scenarios of physical interest, including different spacetime dimensions, other matter fields, or even for a different spacetime causal structure.

ACKNOWLEDGMENTS

The authors thank Carsten Gundlach, Sascha Husa, Esperanza López, and Ulrich Sperhake for discussions on different aspects of this work. The authors acknowledge the high-performance computing resources provided by the Consorci de Serveis Universitaris de Catalunya (CSUC) and the Galicia Supercomputing Center (CESGA) under Projects No. ICTS-CESGA-249 and No. ICTS-CESGA-266. They also acknowledge support from Contracts No. ESP2013-47637-P and No. ESP2015-67234-P (Spanish Ministry of Economy and Competitivity of Spain, MINECO). D. S. acknowledges support from a FPI doctoral Contract No. BES-2012-057909 from MINECO.

APPENDIX A: HYPERBOLIC STRUCTURE OF THE SCALAR FIELD EQUATIONS

The PSC method used for the numerical implementation of the Cauchy evolution requires a first-order hyperbolic formulation of the scalar field equation, the Klein-Gordon Eq. (3). This equation, for the metric in Eq. (4), becomes the following second-order PDE:

$$\ddot{\phi} - A^2 e^{-2\delta}\phi'' = \frac{\dot{A}}{A}\dot{\phi} - \dot{\delta}\dot{\phi} + A e^{-2\delta}\phi' A' - A^2 e^{-2\delta}\delta'\phi' + (d-1)\frac{A^2 e^{-2\delta}}{\cos x \, \sin x}\phi'. \tag{A1}$$

To reduce the order of the equation, we introduce the variables

$$\Pi = \dot{\phi}, \qquad \Phi = \phi'. \tag{A2}$$

The equations for $\boldsymbol{W} = (\phi, \Pi, \Phi)$ constitute a first-order system of PDEs that can be derived from these definitions and from Eq. (A1),

$$\dot{\phi} = \Pi, \tag{A3}$$

$$\dot{\Pi} - A^2 e^{-2\delta}\Phi' = \frac{\dot{A}}{A}\Pi - \dot{\delta}\Pi + A e^{-2\delta}A'\Phi - A^2 e^{-2\delta}\delta'\Phi + (d-1)\frac{A^2 e^{-2\delta}}{\cos x \, \sin x}\Phi, \tag{A4}$$

$$\dot{\Phi} - \Pi' = 0. \tag{A5}$$

As expected, this is a set of first-order PDEs that admits the following compact form:

$$\partial_t \boldsymbol{W} + \mathcal{A}[x, \boldsymbol{W}] \cdot \partial_x \boldsymbol{W} = \boldsymbol{S}[x, \boldsymbol{W}], \tag{A6}$$

where $\mathcal{A}$ is a matrix, and $\boldsymbol{S}$ a vector that depend on the radial coordinate x and our variables $\boldsymbol{W}$, but they do not depend explicitly on the time t. Here, the metric functions δ and A have to be taken as functionals of our variables $\boldsymbol{W}$ since they are the result of integrating Eqs. (12) and (13). From Eqs. (A3)–(A5), the components of the matrix $\mathcal{A}$ are

$$\mathcal{A} = \begin{pmatrix} 0 & 0 & 0 \\ 0 & 0 & -A^2 e^{-2\delta} \\ 0 & -1 & 0 \end{pmatrix}, \tag{A7}$$

and the components of the vector $\boldsymbol{S}$ are

$$\boldsymbol{S} = \begin{pmatrix} \Pi \\ \frac{\dot{A}}{A}\Pi - \dot{\delta}\Pi + A e^{-2\delta} A' \Phi \\ -A^2 e^{-2\delta}\delta' \Phi + (d-1)\frac{A^2 e^{-2\delta}}{\cos x \, \sin x}\Phi \\ 0 \end{pmatrix}. \tag{A8}$$

The characteristic structure of this hyperbolic system of first-order PDEs is determined exclusively by the matrix $\mathcal{A}$ (see, e.g., [18] for details), in such a way that the eigenvectors of $\mathcal{A}$ correspond to the different characteristic fields of the system and the eigenvalues to the characteristic speeds associated with the eigenvectors. Strongly hyperbolic systems are those that have a complete set of eigenvalues and eigenvectors (see, e.g., [18,23,32] for a description of PDEs with hyperbolic structure), which is a key property for showing existence and uniqueness of solutions and also a condition for the stability of algorithms to evolve the system. To find out what happens in our case, we have to solve the eigenvalue problem

$$\mathcal{A}\boldsymbol{E} = \sigma \boldsymbol{E}, \tag{A9}$$

where $\boldsymbol{E}$ is any vector in the space $\{(\phi, \Pi, \Phi)\}$. By analyzing Eq. (A9), we find that we have a complete set of real eigenvalues and eigenvectors; so our system is strongly hyperbolic, as expected for a system of PDEs that is equivalent to the Klein-Gordon equation. The resulting set of eigenvalues and eigenvectors for is

$$\sigma_1 = 0 \longrightarrow \boldsymbol{E}_1 = (1, 0, 0), \tag{A10}$$

$$\sigma_2 = +A e^{-\delta} \longrightarrow \boldsymbol{E}_2 = (0, -A e^{-\delta}, 1), \tag{A11}$$

$$\sigma_3 = -A e^{-\delta} \longrightarrow \boldsymbol{E}_3 = (0, +A e^{-\delta}, 1). \tag{A12}$$

The meaning of the eigenvalues is that they are the characteristic speeds of the characteristic variables. Then, we have a quantity, ϕ, that does not propagate (or in other words, it propagates with zero speed) and two that propagate with speed $\pm v \equiv \pm A e^{-\delta}$ [this is the same speed defined in Eq. (45)]. We can diagonalize the matrix $\mathcal{A}$ by the matrix transformation $\mathcal{A} = \mathcal{K} \cdot \mathcal{D}_{\mathcal{A}} \cdot \mathcal{K}^{-1}$, where $\mathcal{D}_{\mathcal{A}} = \mathrm{diag}(0, v, -v)$ and $\mathcal{K} = (\boldsymbol{E}_1, \boldsymbol{E}_2, \boldsymbol{E}_3)$. At this point, we can define a new set of variables $\boldsymbol{Y}$ as follows: $\boldsymbol{Y} = \mathcal{K}^{-1} \cdot \boldsymbol{W}$. We can see that the principal part of our set of equations becomes completely decoupled for the variables $\boldsymbol{Y}$. These are the characteristic variables. The first one is ϕ, with zero associated propagation speed (eigenvalue), and the other two are

$$Y_+ = \Phi - \frac{\Pi}{v}, \tag{A13}$$

$$Y_- = \Phi + \frac{\Pi}{v}. \tag{A14}$$

The characteristic variable Y_+ propagates with speed v and Y_- with speed $-v$, respectively. Since $v > 0$, Y_+ is a field propagating to the right with speed v, and Y_- is a field propagating to the left with the same speed. From these characteristic variables, we have introduced the variables in Eqs. (5), (6), and (7), which are also characteristic variables, as seen from the evolution Eqs. (8)–(10). Actually, we can see that

$$U = \frac{Y_+}{\cos^{d-2} x}, \qquad V = \frac{Y_-}{\cos^{d-2} x}. \tag{A15}$$

The use of these variables is very important in this work for several reasons but mainly in order to use the PSC method with a multidomain grid. The communication between subdomains becomes very clear in terms of the characteristic variables.

APPENDIX B: BASIC INGREDIENTS OF THE PSC METHOD

Broadly speaking, spectral methods can approximate solutions of PDEs by finite expansions of the variables using a given basis of functions. The coefficients of the expansion are determined by imposing an appropriate criterium that forces this expansion to approach the exact solution as we increase the number of terms. In the case of the PSC method, the criterium consists of imposing the expansion to be exact at a set of *collocation* points (see, e.g., [27–29]). Here, we use the Chebyshev polynomials, $\{T_n(X)\}$ ($X \in [-1, 1]$, the *spectral* domain), as the basis functions, which can be expressed in the following form:

$$T_n(X) = \cos\left(n \cos^{-1}(X)\right). \tag{B1}$$

They are orthogonal in the *continuum* in the following sense:

$$(T_n, T_m) = \int_{-1}^{1} \frac{dX}{\sqrt{1-X^2}} T_n(X) T_m(X) = \frac{\pi c_n}{2} \delta_{nm}, \quad \text{(B2)}$$

where the coefficients c_n are

$$c_n = \begin{cases} 2 & \text{for} \quad n = 0, \\ 1 & \text{otherwise.} \end{cases} \quad \text{(B3)}$$

The set of collocation points that we use are those of a *Lobatto-Chebyshev* grid. The spectral coordinates of these points are the zeros of the polynomial $(1-X^2)T'_N(X) = 0$, where the prime here indicates differentiation with respect to X. The zeros can be written as

$$X_i = -\cos\left(\frac{\pi i}{N}\right) \quad (i = 0, 1, \ldots, N), \quad \text{(B4)}$$

which means that the boundary points $X = \pm 1$ are included in the grid, in contrast with other collocation grids, like for instance the *Gauss-Chebyshev* grid (see, e.g., [27]). Taking into account the properties of the Gauss-Lobatto-Chebyshev quadratures (see, e.g., [27]), the Chebyshev polynomials have another orthogonality relation, in the *discrete*, in the following sense ($n, m = 0, \ldots, N$):

$$[T_n, T_m] = \sum_{i=0}^{N} w_i T_n(X_i) T_m(X_i) = \nu_n^2 \delta_{nm}, \quad \text{(B5)}$$

where w_i are the weights associated with the Chebyshev-Lobatto grid, $w_i = \pi/(N\bar{c}_i)$, and where the $\bar{c}_i$'s are normalization coefficients given by

$$\bar{c}_i = \begin{cases} 2 & \text{for} \quad i = 0, N, \\ 1 & \text{otherwise.} \end{cases} \quad \text{(B6)}$$

Finally, the constants ν_n in Eq. (B5) are given by $\nu_n^2 = \pi \bar{c}_n/2$.

In general, the computational domain, say $[x_L, x_R]$, does not coincide with the spectral one, $[-1, 1]$, and we need a one-to-one mapping between them. The simplest choice, and the one we use, is the linear mapping

$$x \longrightarrow X(x) = \frac{2x - x_L - x_R}{x_R - x_L}. \quad \text{(B7)}$$

and the inverse one is

$$X \longrightarrow x(X) = \frac{x_R - x_L}{2} X + \frac{x_L + x_R}{2}. \quad \text{(B8)}$$

For mesh refinement purposes (see Sec. III B), we use a multidomain PSC method consisting of the division of the computational domain, $\Omega = [x_L, x_R]$, into D disjoint subdomains

$$\Omega = \bigcup_{a=1}^{D} \Omega_a, \quad \Omega_a = [x_{a,L}, x_{a,R}], \quad \text{(B9)}$$

where $x_{a,L}$ and $x_{a,R}$ are the left and right boundaries of the subdomain Ω_a ($x_{1,L} = x_L$ and $x_{D,R} = x_R$). Since they are disjoint subdomains, we have $x_{a,L} = x_{a-1,R}$ ($a = 1, \ldots, D$). We apply the PSC method to each subdomain, and hence, our variables have different expansions in Chebyshev polynomials in each subdomain. Then, each *physical* subdomain is mapped to the *spectral* domain $[-1, 1]$ using the linear mappings of Eqs. (B7) and (B8), which we call $x_a(X)$ and $X_a(x)$. The different expansion for the different subdomains are then *matched* by using the appropriate boundary conditions (see the description in Sec. III A).

Let us now look at the spectral approximation for the variables of our problem, which we arranged in the vector $\boldsymbol{Z}$. At a given subdomain Ω_a, in the PSC method, we have two representations of the approximation for our variables. First, we have the standard spectral representation of the approximation to our variables, $\boldsymbol{U}_{a,N}(t, x)$,

$$\boldsymbol{U}_{a,N}(t, x) = \sum_{n=0}^{N} \boldsymbol{a}_{a,n}(t) T_n(X_a(x)), \quad \text{(B10)}$$

where the $\boldsymbol{a}_{a,n}$ are (time-dependent) vectors that contain the spectral coefficients of the expansion of our variables. In the PSC method, we have also a *physical* expansion, which looks as follows:

$$\boldsymbol{U}_{a,N}(t, x) = \sum_{i=0}^{N} \boldsymbol{U}_{a,i}(t) \mathcal{C}_i(X_a(x)), \quad \text{(B11)}$$

where $\mathcal{C}_i(X)$ are the *cardinal* functions [27] associated with our choice of basis functions (Chebyshev polynomials) and set of collocation points (Lobatto-Chebyshev grid). Their expression is

$$\mathcal{C}_i(X) = \frac{(1-X^2)T'_N(X)}{(1-X_i^2)(X - X_i)T''_N(X_i)}. \quad \text{(B12)}$$

The cardinal functions have the following remarkable property:

$$\mathcal{C}_i(X_j) = \delta_{ij} \quad (i, j = 0, \ldots, N), \quad \text{(B13)}$$

so that the time-dependent (vector) coefficients, $\{\boldsymbol{U}_i\}$, of the expansion in Eq. (B11) are the values of our variables at the collocation points

$$\boldsymbol{U}_{a,N}(t, x_a(X_i)) = \boldsymbol{U}_{a,i}(t). \quad \text{(B14)}$$

These are the unknowns that one looks for in the PSC method. The spectral and physical representations [Eqs. (B10) and (B11), respectively] are related via a matrix transformation [27]. The computations (float-point

operations) required to change representation using the matrix transformations increase with the number of collocation points as $\sim N^2$. Nevertheless, we can introduce a new spectral coordinate via $X = \cos\theta$ (with $\theta \in [0, \pi]$) in such a way that the Chebyshev polynomials become a trigonometrical function,

$$T_n(\cos\theta) = \cos(n\theta). \tag{B15}$$

As a consequence, an spectral expansion in Chebyshev polynomials like the one in Eq. (B10) can be mapped to a cosine series. We can then perform the change of representation by means of a discrete Fourier transform using a fast-Fourier transform (FFT) algorithm. In our numerical codes, we use the routines of the FFTW library [40]. Then, the number of computations required for a change in representation increases as $\sim N \ln N$ with the number of collocation points.

Changing between representations is useful in order to compute derivatives and nonlinear terms. In the case of derivatives, it is simpler to compute them in the spectral representation. Then, we can transform from the physical to the spectral representation, compute derivatives there, and finally transform back to the physical representation. In the case of a Chebyshev PSC method, the differentiation process can be described by the following scheme:

$$\partial_x : \{\boldsymbol{U}_i\} \xrightarrow{FFT} \{\boldsymbol{a}_n\} \xrightarrow{\partial_x} \{\boldsymbol{b}_n\} \xrightarrow{FFT} \{(\partial_x \boldsymbol{U})_i\}, \tag{B16}$$

where $\{\boldsymbol{b}_n\}$ are the spectral coefficients associated with the spatial derivative ∂_x, and their relation to the spectral coefficients of the variables, $\{\boldsymbol{a}_n\}$, is given by (see, e.g., [27])

$$\boldsymbol{b}_N = \boldsymbol{b}_{N-1} = 0, \tag{B17}$$

$$\boldsymbol{b}_{n-1} = \frac{1}{c_n}\{2n\boldsymbol{a}_n + \boldsymbol{b}_{n+1}\} \quad (n = N-1, \ldots, 1), \tag{B18}$$

where the coefficients c_n are given in Eq. (B3).

Another important operation where changing the representation is very useful is integration. Let us assume we want to integrate the function $g(X)$ (we assume we have already changed to the spectral coordinate X) from the right, that is, $f(X) = \int_X^{X_N=1} dX' g(X')$, which assumes that an integration constant/boundary condition is imposed on the right boundary, $f(X_N) = f_N$. Then, we can follow the scheme

$$\int_X^1 : \{\boldsymbol{U}_i\} \xrightarrow{FFT} \{\boldsymbol{a}_n\} \xrightarrow{\partial_x} \{\boldsymbol{b}_n\} \xrightarrow{FFT} \left\{\left(\int_X^1 \boldsymbol{U}\right)_i\right\}, \tag{B19}$$

where $\{b_n\}$ are the spectral coefficients associated with the integral from the right, $f(X)$, and their relation to the spectral coefficients of the function $g(X)$, $\{a_n\}$, is given by

$$b_N = \frac{a_{N-1}}{2N}, \tag{B20}$$

$$b_n = \frac{1}{2n}\{\bar{c}_{n-1}a_{n-1} - a_{n+1}\} \quad (n = N-1, \ldots, 1), \tag{B21}$$

$$b_0 = f_N - \sum_{n=1}^{N} b_n. \tag{B22}$$

The process to integrate from the left, $f(X) = \int_{X_0=-1}^{X} dX' g(X')$, is very similar. In this paper, we use both since some variables that we obtain via integration with respect to x require a boundary condition at the origin and others on the AdS boundary. It is simple to extend these rules to our multidomain scheme.

Finally, in the PSC method, we find a discretization of our system of equations in Eqs. (8)–(13) by imposing them at every collocation point. In practice, this is done by introducing the expansion (B11) into the Eqs. (8)–(13), and then we evaluate the result at every collocation point of our Chebyshev-Lobatto grid (B4). We obtain a system of ODEs for the variables $\{\boldsymbol{U}_i(t)\}$,

$$\dot{\boldsymbol{U}}_i = \mathbb{A} \cdot (\partial_x \boldsymbol{U})_i + \mathbb{B} \cdot \boldsymbol{U}_i + \boldsymbol{S}_i, \tag{B23}$$

where the dot denotes differentiation with respect to the time coordinate, t, and $(\partial_x \boldsymbol{U})_i$ has to be interpreted according to the scheme in Eq. (B16).

[1] M. W. Choptuik, Universality and Scaling in Gravitational Collapse of a Massless Scalar Field, Phys. Rev. Lett. **70**, 9 (1993).

[2] C. Gundlach, The Choptuik Space-Time as an Eigenvalue Problem, Phys. Rev. Lett. **75**, 3214 (1995).

[3] C. Gundlach and J. M. Martin-Garcia, Critical phenomena in gravitational collapse, Living Rev. Relativity **10**, 5 (2007).

[4] P. Bizoń and A. Rostworowski, On Weakly Turbulent Instability of Anti-de Sitter Space, Phys. Rev. Lett. **107**, 031102 (2011).

[5] J. Jałmużna, A. Rostworowski, and P. Bizoń, A comment on AdS collapse of a scalar field in higher dimensions, Phys. Rev. D **84**, 085021 (2011).
[6] M. Maliborski, Instability of Flat Space Enclosed in a Cavity, Phys. Rev. Lett. **109**, 221101 (2012).
[7] H. Okawa, V. Cardoso, and P. Pani, Collapse of self-interacting fields in asymptotically flat spacetimes: Do self-interactions render Minkowski spacetime unstable?, Phys. Rev. D **89**, 041502 (2014).
[8] H. Okawa, V. Cardoso, and P. Pani, Study of the nonlinear instability of confined geometries, Phys. Rev. D **90**, 104032 (2014).
[9] R.-G. Cai and R.-Q. Yang, Scaling laws in gravitational collapse, arXiv:1512.07095.
[10] V. Cardoso and J. V. Rocha, Collapsing shells, critical phenomena and black hole formation, Phys. Rev. D **93**, 084034 (2016).
[11] R.-G. Cai and R.-Q. Yang, Multiple critical gravitational collapse of charged scalar with reflecting wall, arXiv :1602.00112.
[12] V. Husain, G. Kunstatter, B. Preston, and M. Birukou, Anti-de Sitter gravitational collapse, Classical Quantum Gravity **20**, L23 (2003).
[13] D. S. Goldwirth and T. Piran, Gravitational collapse of massless scalar field and cosmic censorship, Phys. Rev. D **36**, 3575 (1987).
[14] D. Santos-Oliván and C. F. Sopuerta, New Features of Gravitational Collapse in Anti-de Sitter Spacetimes, Phys. Rev. Lett. **116**, 041101 (2016).
[15] M. W. Choptuik, T. Chmaj, and P. Bizon, Critical Behavior in Gravitational Collapse of a Yang-Mills Field, Phys. Rev. Lett. **77**, 424 (1996).
[16] P. R. Brady, C. M. Chambers, and S. M. C. V. Goncalves, Phases of massive scalar field collapse, Phys. Rev. D **56**, R6057 (1997).
[17] A. Buchel, L. Lehner, and S. L. Liebling, Scalar collapse in AdS, Phys. Rev. D **86**, 123011 (2012).
[18] R. Courant and D. Hilbert, *Methods of Mathematical Physics*, Vol. II (John Wiley & Sons, New York, 1989).
[19] R. Arnowitt, S. Deser, and C. W. Misner, in *Gravitation: An Introduction to Current Research*, edited by L. Witten (John Wiley & Sons, New York, 1962), pp. 227–265.
[20] D. Garfinkle, Choptuik scaling in null coordinates, Phys. Rev. D **51**, 5558 (1995).
[21] J. Bland, B. Preston, M. Becker, G. Kunstatter, and V. Husain, Dimension dependence of the critical exponent in spherically symmetric gravitational collapse, Classical Quantum Gravity **22**, 5355 (2005).
[22] J. Bland and G. Kunstatter, The 5-D Choptuik critical exponent and holography, Phys. Rev. D **75**, 101501 (2007).
[23] F. John, *Partial Differential Equations* (Springer Verlag New York, Inc., New York, 1991).
[24] P. Canizares and C. F. Sopuerta, An efficient pseudospectral method for the computation of the self-force on a charged particle: Circular geodesics around a Schwarzschild black hole, Phys. Rev. D **79**, 084020 (2009).
[25] P. Canizares, C. F. Sopuerta, and J. L. Jaramillo, Pseudospectral collocation methods for the computation of the self-force on a charged particle: Generic orbits around a Schwarzschild black hole, Phys. Rev. D **82**, 044023 (2010).
[26] P. Canizares and C. F. Sopuerta, Tuning time-domain pseudospectral computations of the self-force on a charged scalar particle, Classical Quantum Gravity **28**, 134011 (2011).
[27] J. P. Boyd, Chebyshev and Fourier Spectral Methods, 2nd ed. (Dover, New York, 2001).
[28] B. Fornberg, *A Practical Guide to Pseudospectral Methods* (Cambridge University Press, Cambridge, England, 1996).
[29] C. Canuto, A. Quarteroni, M. Y. Hussaini, and T. A. Zang, *Spectral Methods. Fundamentals in Single Domains* (Springer-Verlag, Berlin, 2006).
[30] J. C. Butcher, *Numerical Methods for Ordinary Differential Equations* (John Wiley & Sons, Chichester, 2003).
[31] W. H. Press, B. P. Flannery, S. A. Teukolsky, and W. T. Vetterling, *Numerical Recipes: The Art of Scientific Computing* (Cambridge University Press, Cambridge, England, 1992).
[32] B. Gustafsson, H. Kreiss, and J. Oliger, *Time Dependent Problems* (John Wiley & Sons, New York, 1995).
[33] B. Gough, *GNU Scientific Library Reference Manual*, 3rd ed. (Network Theory Ltd., Surrey, 2009).
[34] D. Garfinkle and G. C. Duncan, Scaling of curvature in subcritical gravitational collapse, Phys. Rev. D **58**, 064024 (1998).
[35] C. Gundlach, Understanding critical collapse of a scalar field, Phys. Rev. D **55**, 695 (1997).
[36] S. Hod and T. Piran, Fine structure of Choptuik's mass scaling relation, Phys. Rev. D **55**, R440 (1997).
[37] J. Abajo-Arrastia, E. da Silva, E. Lopez, J. Mas, and A. Serantes, Holographic relaxation of finite size isolated quantum systems, J. High Energy Phys. 05 (2014) 126.
[38] E. da Silva, E. Lopez, J. Mas, and A. Serantes, Collapse and revival in holographic quenches, J. High Energy Phys. 04 (2015) 038.
[39] C. Gundlach (private communication).
[40] M. Frigo and S. G. Johnson, The design and implementation of FFTW3, Proc. IEEE **93**, 216 (2005).